Predicting Xenon Oscillations in PWRs using Intrusive Reduced Order Modelling

Kristoffer Tofveson Pedersen

Division of Subatomic, High Energy and Plasma Physics
Department of Physics
Chalmers University of Technology
SE-412 96 Göteborg
Sweden
September 1, 2023

Predicting Xenon Oscillations in PWRs using Intrusive Reduced Order Modelling

KRISTOFFER T. PEDERSEN

Cover: Xenon periodic table illustration.

Predicting Xenon Oscillations in PWRs using Intrusive Reduced Order
Modelling
Kristoffer T. Pedersen
Division of Subatomic, High Energy and Plasma Physics
Department of Physics
Chalmers University of Technology

Abstract

The increasing presence of intermittent energy sources in the Swedish electricity grid necessitates a transition of Swedish nuclear reactors from constant base load operation to load-following mode. However, such changes in power can induce xenon oscillations, a phenomenon that poses operational challenges and the risk of fuel damage. Xenon oscillations occur due to the decay characteristics of iodine-135 and xenon-135 produced in the fission process, exhibiting a periodicity of 15 to 30 hours. Detecting these oscillations proves challenging as they may result in localized power variations while the overall power of the reactor core remains relatively stable.

This thesis aims to develop a computationally efficient and transparent model capable of predicting the susceptibility of nuclear reactors to unstable xenon oscillations. Two models are created and assessed: a simple physics-transparent model based on a one-group homogeneous core representation, and a more involved model, which incorporates two energy groups and a heterogeneous spatial discretization with nodal resolution.

Comparative analysis of the models reveals notable disparities in predicting instabilities related to xenon oscillations. The number of energy groups emerges as the primary factor contributing to the discrepancies observed. Moreover, spatial resolution is critical in capturing eigenmode coupling when spatial offsets exist in the equilibrium neutron flux distribution. It is demonstrated that the latter model indicates a higher level of system instability concerning xenon oscillations.

The findings underscore the significance of considering both spatial and energy resolution to accurately assess the stability of the system.

List of Publications

Paper I

Kristoffer T. Pedersen and Christophe Demazierè and Paolo Vinai. "A Three-Dimensional Two-Energy Group Heterogeneous Intrusive Reduced Order Model of Xenon Oscillations in PWRs". en. In: *International Conference on Mathematics and Computational Methods Applied to Nuclear Science and Engineering.* (Aug 2023). At: Niagara Falls, Ontario.

Paper II

Kristoffer T. Pedersen and Christophe Demazierè and Paolo Vinai. "Understanding Xenon Oscillations Through Physics-Based Reduced Order Modelling". In: *American Nuclear Society Annual Meeting* (June 2022). At: Anaheim, LA. (PP. 772-775). *126.*

The author's contribution to the included papers Paper I and Paper II: Kristoffer T. P. developed all the Matlab and Mathematica codes for computation, performed all the simulation work, and generated the plots and the tables included in the paper. The development of the theoretical concepts, the interpretation of the results, and the writing of the papers was done in collaboration with the co-authors.

Acknowledgements

I would like to thank my family and my wife for all their love, support and encouragement during all my years of studying.

Finally, I would like to send my love to my wife, Amanda, and my daughter, Frigga, and express my heartfelt gratitude for their companionship on this adventure abroad.

Contents

List of Figures

List of Tables

1

Introduction

1.1 Background

Nuclear power currently accounts for 10% of global electricity demand, positioning it as the second-largest source of low-carbon electricity worldwide, following hydropower [1]. Alongside other clean energy sources such as hydro, wind, and solar power, nuclear power offers significant potential to generate low-carbon electricity and combat climate change. Notably, nuclear and hydropower are considered stable and controllable energy sources, as long as fuel e.g., fissile material and water reserves, is available. These sources are called baseload sources. On the other hand, the generation of wind and solar power varies with the local weather. These sources are called intermittent energy sources. There is a notable expansion in the deployment of wind and solar power, as outlined in the International Energy Agency's (IEA) 2022 roadmap for achieving net-zero greenhouse gas emissions. According to the roadmap, renewable sources are projected to generate 60% of global electricity by 2030 [2]. Within this framework, nuclear power is expected to undergo a fourfold increase by 2050. In grids with high penetration of intermittent energy sources, operating nuclear power reactors often necessitates a transition from baseload mode to load-following mode. This shift enables compensation for fluctuations in the variable output of other energy sources.

Specifically, the Swedish electricity mix has, historically, been comprised of 50% hydro and 50% nuclear power. Over the past two decades, the proportion of wind power has risen to 17%, while the share of nuclear power has reached 35% due to several reactor closures [3]. The increasing presence of intermittent energy sources implies that Swedish nuclear reactors might need to shift from baseload mode to load-following mode [4, 5]. Although the Swedish reactors were originally designed for flexible operation, they have not operated in this mode for the past 20 years [4, 5]. Consequently, extensive analysis and validation work is necessary for the reactors to resume operating in this manner [5].

This research aims to develop a tool for a comprehensive analysis of the reactor's ability to operate in a flexible load-following mode, focusing on a critical phenomenon known as xenon oscillations. The study aims to develop an effective and physics-transparent method for predicting possible xenon oscillations in nuclear reactors.

1.2   The Neutron Cycle

To better understand the effect of xenon in a nuclear reactor, the so-called neutron cycle is briefly introduced. Inside the core of nuclear power reactors, fissile material undergoes fission reactions to produce energy. For each fission reaction, a neutron is absorbed by a fissile nucleus, such as uranium-235, which subsequently splits into two smaller nuclei and releases energy as well as a number of new neutrons. These neutrons can be absorbed into other fissile nuclei and thereby create a chain reaction. In most commercial thermal nuclear reactors, water around the fuel is used as a moderator. The moderator thermalises the neutrons, making it much more likely that they will cause a fission reaction in the fuel, which consists of low-enriched uranium.

The neutron cycle consists of several sources and sinks visualised in Fig. 1.1. These gains and losses through the neutron cycle must be balanced for the reactor to be at equilibrium and thus produce a constant power output. The steps in the neutron cycle are:

- Fast neutrons are created from thermal and fast fissions.

- The neutrons can be lost before slowing down.

- While slowing down, the neutrons can be absorbed in the U-238 resonances.

- After thermalisation the neutron can escape the reactor or be absorbed in other materials than the fuel.

- After absorption in the fuel, it is not certain that the neutron will cause a new fission event.

- The remaining neutrons are absorbed into fissile material and produce new fission events

Xenon poisoning increases the absorption of thermal neutrons in materials other than fuel and thereby causes an imbalance in the neutron cycle. This process will be further explained in the next section.

1.3   Xenon Poisoning

1.3.1   Physics of xenon poisoning

Xe-135 is created from two paths. A small fraction is produced directly as a fission product while the main way of its creation is as a decay product of the fission product Te-135, which quickly decays to I-135 and then to Xe-135 as shown in Fig. 1.2. The two possible ways that xenon can be removed are either by neutron capture where it becomes xenon-136, which is stable and has a low neutron cross section, or by natural decay to Caesium-135, which has a much longer half-life than Xe-135 and also a relatively low neutron capture cross section.

As can be seen in Fig. 1.3, the absorption cross section at thermal energies for Xe-135 is more than six orders of magnitude higher than that of U-238 at thermal energies, shown in
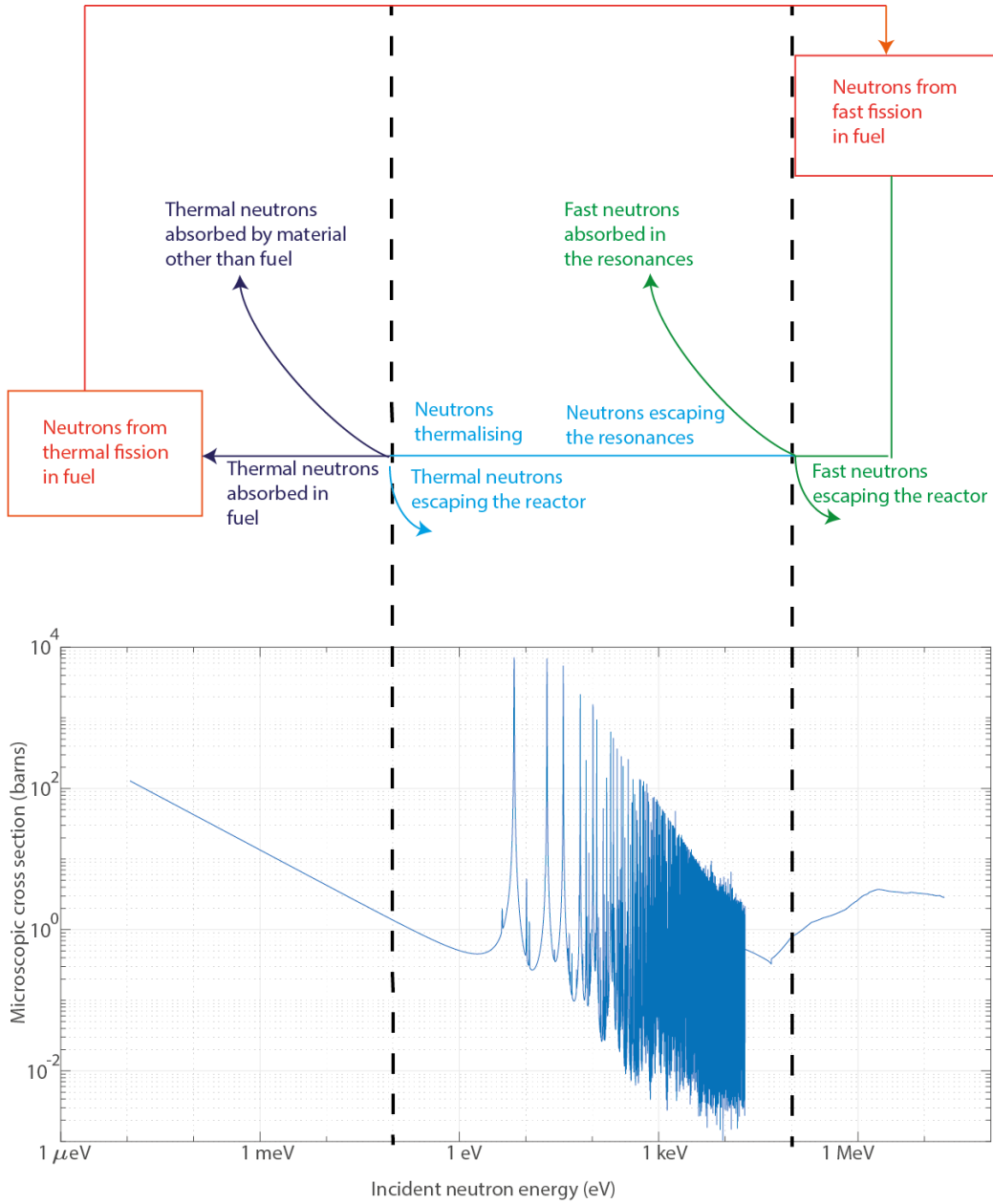
Figure 1.1: Neutron cycle and neutron absorption cross section of U-238 as a function of incident neutron energy. Figure inspired by [6] and with data from [7].
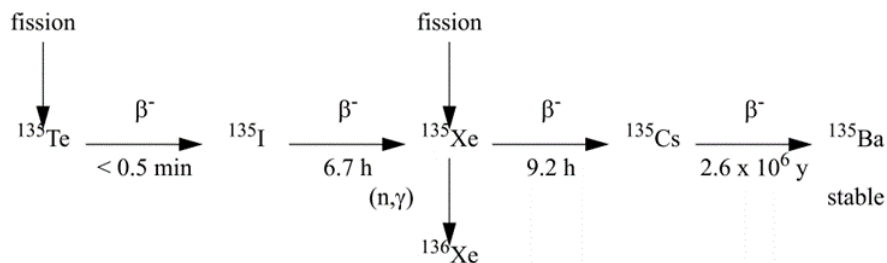
Figure 1.2: Sources and sinks of xenon-135 in a nuclear reactor taken from [6].
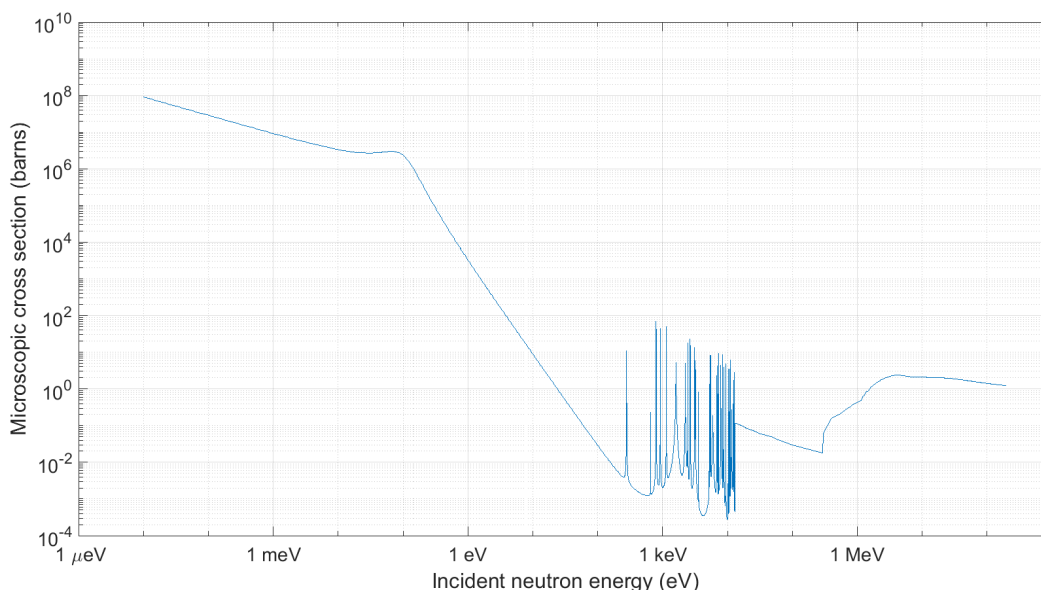
Figure 1.3: Xenon absorption cross section as a function of neutron energy

Fig. 1.1.

Some time after the startup of a nuclear power plant, the xenon concentration will reach equilibrium as it is continuously produced from iodine decays and fission and is being lost at the same rate through decay and neutron absorption.

In a one-energy group homogenous reactor model, the equilibrium iodine- and xenon concentration is written as:

$$I_{eq}(\mathbf{r}) = \frac{\gamma_I \Sigma_f \phi_{eq}(\mathbf{r})}{k_{eff} \lambda_I} \tag{1.1}$$

$$X_{eq}(\mathbf{r}) = \frac{(\gamma_I + \gamma_X) \Sigma_f \phi_{eq}(\mathbf{r})}{k_{eff}(\lambda_X + \sigma_X \phi_{eq}(\mathbf{r}))} \tag{1.2}$$

With Σ_f being the macroscopic fission cross section, k_{eff} being the effective multiplication factor, λ_X, λ_I, γ_X and γ_I being the decay constants and branching ratios of Xe-135 and

I-135 respectively, σ_X being the microscopic neutron absorption cross section for Xe-135 and $\phi_{eq}(\mathbf{r})$ being the equilibrium neutron flux distribution within the core. The definitions of these parameters are standard to the field and can be found in any reactor physics textbook [6, 8]. They will therefore not be further explained in this work.

After a reactor shutdown, the large reduction of neutron absorption and the faster decay of I-135 compared to Xe-135 will cause the xenon level in the reactor to rise for a period. During this period the negative reactivity due to xenon might exceed the available reactivity from control rod withdrawal or dilution of the boric acid within the reactor. This might leave the reactor inoperable for an extended period of time called *xenon dead time*.

1.3.2 Dynamics of xenon oscillations

In large reactors with low neutronic coupling, small asymmetric disturbances in the neutron flux can lead to non-uniform concentrations of Xe-135 within regions of the core. The initial loss of symmetry can be caused by, for example, control rod insertions. This leads to differences in the flux level, which causes local power oscillations within the core over time. From an initial perturbation, where the flux is lowered at the top of the core and increased at the bottom of the core, the mechanism can be described in four steps.

- An initial lack of symmetry within the core flux distribution causes an imbalance in the I-135 buildup and the Xe-135 absorption between regions in the core.

- In the high flux region, iodine is produced, and xenon is burned off at a higher rate. This further increases power. In the low-flux region, iodine is produced at a lower rate and xenon is not burned off. This further lowers the flux in the region.

- As the iodine decays, the production of xenon increases in the high-flux region, this increases neutron absorption and lowers the flux. Simultaneously the xenon in the low-flux region starts to decay which decreases the absorption, thereby increasing the flux. Thus, the high flux and low flux regions swap between the top and bottom.

- This cycle may repeat itself with periods of around 15-30 hours [8, 9]. Under certain core configurations, the difference between the top and bottom regions may increase over time.

Because of a low shift in the overall power level of the core and because of the long oscillation period, xenon oscillations can be hard to detect by operators but can result in local power levels increasing by a factor of three or more [8]. Such an increase in power poses a threat to reactor operation and fuel integrity. While oscillations in the radial plane can occur due to misalignment of control rods or sudden shifts in power faster than the xenon iodine decay time scale [8], most of these tend to be stable meaning that the amplitude of the oscillations decay over time. The stability of axial oscillations, on the other hand, depends on burnup, power level and the core configuration among other things [10–13].

For this reason, it is of utmost importance that efficient and transparent models are developed

to predict core configurations that lead to the occurrence of unstable xenon oscillations.

1.3.3   Historic significance of xenon poisoning in nuclear power reactors

At the dawn of reactor physics in 1944, the United States was developing a nuclear weapon in an arms race against Germany, which was further accelerated by the Japanese attack on Pearl Harbour. As a part of this, the third and largest nuclear reactor ever built was constructed at a site near Richland, Washington. The site was named the Hanford site and the project was called the B reactor. It was a 250MW graphite-moderated and water-cooled reactor to produce plutonium which would fuel the atomic bomb that was dropped on Nagasaki in 1945 [14, 15]. Initially, the reactor was supposed to be built with 1,500 process tubes for inserting uranium fuel and later extracting it for post-processing. However, a physicist named John Wheeler had expressed concerns that the nuclear reactions might create neutron-absorbing by-products, which made the engineer George Graves insist that the reactor instead should include 2,004 process tubes [16].

As it turned out, when the reactor was first made critical, everything seemed fine at first. The operators drew out the control rods in increments to increase the power to full but once the reactor reached 9 MW the power stopped rising and the reactor soon became subcritical again. John Wheeler and Enrico Fermi worked together and showed that xenon-135 was the culprit of the stalled reactor. It was determined that additional uranium fuel was needed and by utilising every one of the 2,004 process tubes the reactor could be brought to full power. Had the design not accounted for the possibility of a reactor poison, it would have faced a major setback [16].

Another significant example illustrating the consequences of xenon poisoning occurred much later in history. On April 25, 1986, during the final years of the Soviet Union, a catastrophic accident took place at the Chernobyl reactor during a shutdown procedure. As part of the procedure, a safety test was conducted to assess the feasibility of utilising the mechanical energy in the turbine to ensure the power requirements during a cutoff of steam supply. During the ramp-down process, the test was momentarily paused when the reactor was operating at half of its nominal power due to an electricity shortage on the grid. However, during this time, the power unexpectedly dropped dramatically due to xenon poisoning of the core. [17]

Instead of terminating the experiment and shutting down the reactor, the chief engineer decided to withdraw absorbers from the core to increase the power output. The withdrawal of absorbers together with the consumption and decay of xenon caused the power level to rise rapidly. Compounding the issue, the low coolant flow rate brought the reactor into an unstable thermo-hydraulic state where it could easily be brought to boiling. This combination of removed absorbers and the unstable state of the coolant water rendered the reactor extremely dangerous [17].

As the power increased at an unexpectedly high pace, the operators tried to fully insert the

safety rods (SCRAM). The insertion of the graphite-tipped rods led to increased moderation in the bottom of the reactor. This, together with the displacement of water which decreased neutron absorption and the shift in neutron flux due to xenon poisoning at the top of the core led to a local increase in reactivity. The subsequent power surge resulted in the boiling of coolant water. Since the core had a positive void coefficient the steam production led to a positive feedback loop causing a massive steam explosion. [18]

It is important to note that the above description provides a surface-level overview of the accident, omitting numerous technical and political factors that contributed to the decision-making process. However, if the chief engineer, Alexander Akimov, had been more aware of the dangers posed by xenon poisoning, it is conceivable that the worst nuclear power disaster in history might have been prevented.

1.3.4 Modelling, Predicting and Avoiding Xenon Oscillations

Free-running xenon oscillations are not allowed in an operating nuclear reactor, except under specific controlled testing conditions [12]. Thus, it is important to predict when a certain reactor configuration will exhibit xenon oscillations and when these could grow in time if not disrupted. This section will go through some of the prediction and control algorithms available as well as the design specifications for nuclear reactors that minimise the risk of xenon oscillations.

1.3.4.1 Design specifications

The largest determining factor in whether a nuclear reactor core exhibits xenon oscillations is its size [13, 19]. Large cores are more susceptible to xenon oscillations since the distances within the core are large compared to the migration length of the thermal neutrons within the core [20]. Such a core has a low degree of neutronic coupling effectively meaning that actions taken at one end of the reactor will have little effect on the other end. A low neutronic coupling allows, for example, the flux to remain high at the bottom of the core even as control rods are inserted at the top. This has the potential to create unstable asymmetries in the xenon-iodine distribution within the core.

Contrary to this, the economy of scale dictates that large reactors have an economic advantage over smaller ones, which often means that the possibility of some xenon oscillations must be accepted for a given design. Indeed, it has been shown that many larger reactor designs such as the AP-1000, VVER-1000 and the CANDU reactors under certain conditions can be unstable with respect to xenon oscillations [12, 21–23].

It has been shown that the relationship between the radius and the height of the reactor has an impact on the stability of nuclear reactors. Obaidurrahman and Singh [13] find that the condition $H/D > 0.92$, with H being the height of the reactor and D being the diameter, should be respected for PWRs to avoid unstable transients. This relationship is related to the separation of eigenvalues which will be covered later in the thesis.
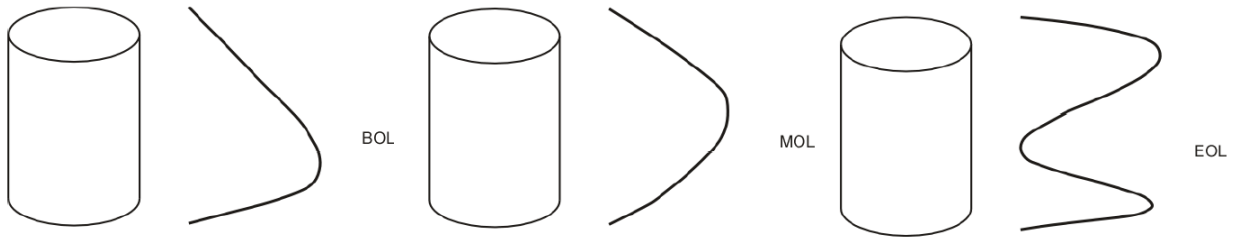
Figure 1.4: Axial flux profile vs. core age [24]

1.3.4.2 Prediction and modelling of xenon oscillations

The problem of modelling xenon oscillations is difficult because it contains a strong non-linear coupling between the neutron flux and the xenon concentration in the core as well as a non-linear thermal-hydraulic coupling. All attempts at modelling the problem depend on simplifications and assumptions. In all deterministic models of the problem, the diffusion approximation has been applied.

An important measure of axial xenon oscillations is the Axial Offset (AO) or Axial Shape Index (ASI) of the power and xenon distribution. The power axial offset is defined as:

$$AO_p = \frac{P_t - P_b}{P_t + P_b} \tag{1.3}$$

i.e., the relative difference in flux between the top and bottom of the core. With P_b and P_t meaning the average power in the bottom and top half of the core, respectively. Likewise, the radial offset (RO) can be defined as the relative difference between one side of the core and the other. Most reactors have some non-zero axial and radial offset even at 100% power and all control rods are withdrawn due to the initial fuel configuration. These measures are called Equilibrium Axial Offset (EAO) and Equilibrium Radial Offset (ERO). Burnup can change these measures over long time periods as visualised in Fig. 1.4 and is shown to also impact the stability of the core with respect to xenon oscillations, with divergent xenon oscillations usually occurring later in core life [12, 24].

The minimum requirement for the solution of the problem is a 2-point reactor kinetics model, where the reactor is split into a top and bottom part with the definition of parameters for the neutronic coupling between the two regions. This method has proven sufficient for calculating the correct axial offset for test-case transients with small errors compared with high-fidelity simulations [10, 25–27].

1.3.4.3 Control

Control during transients is mostly carried out manually by the operator assisted by automatic estimation and prediction of important non-measured states for decision support [27]. Typically bounds are placed on the axial offset to remain within ±5% at most times during

power transients [26]. Load control of a PWR core is usually carried out with a combination of control rod insertion and boron acid injection into the coolant.

Since xenon oscillations are difficult to detect on the overall power output of the core, detectors must be placed at the bottom and at the top of the core to record any deviation between the two values and calculate the axial offset.

An early control strategy is aimed at inserting control rod banks when the flux of the top part of the core is at its maximum to suppress the oscillation corresponding to the first harmonic cosine shape of the flux [28, 29]. This strategy might prove problematic as the local power peak at the maximum amplitude might be outside of regulatory limits for the reactor. Yoichiro [25] proposed a method for continuous guidance for the operator allowing control rod operations to be carried out in much smaller steps.

The field of nuclear reactor control is large and will not be covered in this thesis but many newer schemes, both linear and non-linear, for automated control are being considered ranging from simple proportional-integral-differential (PID) controllers to deep artificial neural networks [27].

1.4 Reduced Order Modelling

1.4.1 Purpose of Reduced Order Modelling

Reduced order modelling (ROM) aims to transform a complex and often non-linear system with many degrees of freedom into a simpler system containing only a few degrees of freedom. This simpler system can be solved at a much lower computational cost while still retaining the essential dynamics and behaviour of the original problem. The method has been applied to various fields within science and engineering and has in recent years seen great advancements driven by greater computational resources and integration of machine learning [30, 31].

Reduced order models can be divided into two groups. Intrusive and non-intrusive ROMs. An intrusive strategy will be the focus of this thesis and obtains the model reduction by transforming the underlying physics equations of the problem into simpler equations with fewer degrees of freedom through mathematical operations and approximations. This approach has the advantage that it does not rely on any additional information about the system such as experimental or high-fidelity model data. Since it is based on the governing equations, the model can also be more transparent to the underlying physics. On the other hand, the governing equations might not be available or might be too complex to manipulate [32, 33].

A non-intrusive strategy focuses on building a reduced order model by capturing the low-order dynamics from full-order model snapshot evaluations of either experiments or high-fidelity models. This approach is usually entirely data-driven and the underlying physics equations are not introduced. It has the advantage of not relying on the governing equations which might not always be available for a complex system. Furthermore, the recent advances in

high fidelity modelling and increase in computer power give a good opportunity for creating the necessary snapshots in many cases [30].

1.4.2   History of Reduced Order Modelling

While the term reduced order modelling has only gained popularity in the later parts of the 20th century, it has roots as far back as the beginning of the 19th century. In 1811, Joseph Fourier presented an article, in which he showed that the problem of calculating the heat transfer in solid bodies could be greatly simplified by postulating the following theorem: *"Any function, continuous or discontinuous, of a variable can be expressed as a series of sines of multiples of the variable"* [31, 34]. This theorem meant that a solution to the heat equation could be expressed in the form of an infinite sum of sine functions. E.g., given the equation:

$$\frac{\partial u(x,t)}{\partial t} = \alpha \frac{\partial^2 u(x,t)}{\partial x^2} \tag{1.4}$$

and the appropriate boundary conditions and initial conditions:

$$u(0,t) = 0 = u(L,t) \tag{1.5}$$
$$u(x,0) = f(x); \qquad \forall x \in [0,L] \tag{1.6}$$

and given that the separation of variables holds, the solution can be written as:

$$u(x,t) = \sum_{n=1}^{\infty} D_n \sin\left(\frac{n\pi x}{L}\right) e^{-\frac{n^2 \pi^2 \alpha t}{L^2}} \tag{1.7}$$

with

$$D_n = 2/L \int_0^L f(x) \sin\left(\frac{n\pi x}{L}\right) \mathrm{d}x \tag{1.8}$$

Each function within the sum is called a basis function or mode. The exponential part of each mode containing $-n^2$ means that higher order modes with larger n decay faster in time than lower order modes. This fact allows truncating the sum to N modes while retaining the essential dynamics of the system. This truncation is convergent such that the error becomes smaller with increasing N [34].

Later, in 1867, William Thompson, also known as Lord Kelvin, was working on the problem of predicting the tides in an efficient manner. Previously this had been done manually by solving Laplace's tidal equations from 1770 [35]. These calculations were based on local observations which were then analysed to derive coefficients related to the tidal components derived from the sun and moon motion. This was an immensely tedious task when done with

pen and paper. Kelvin devised that the tidal signature could be represented by a Fourier series of sine functions each representing different harmonic periods in nature such as the day, month, and year cycle along with many others. These simple sine functions could be recreated mechanically by a machine consisting of a series of gears and pulleys that moved a pen vertically on a moving sheet of paper. Each gear corresponds to a harmonic component of the sine series. His design is shown in Fig. 1.5 including 10 harmonic components of the sine series [35, 36]. This analogue computer is an excellent example of the effectiveness of reduced order modelling, whereby a complicated tidal signal is broken down into N simple functions, each of which can be calculated with relative ease. The method is still applied today, though digitally, and usually includes 37 harmonic components [35].

1.4.3 Spectral Methods

Reduced order modelling is a very wide class of mathematical methods to reduce the degrees of freedom in a problem[30–32].

In Eq. (1.7), it was seen that the solution to the heat equation can be expressed as an infinite sum of a time-dependent exponential function multiplied by a space-dependent sine function multiplied by some mode-specific constant or amplitude. More generally, this can be written as

$$u(x,t) = \sum_{n=1}^{\infty} a_n(t)\phi_n(x) \tag{1.9}$$

This is known as the Galerkin expansion whereby a solution is expanded into an infinite sum of orthogonal space-dependent basis functions which satisfy Eq. (1.5) and (1.6) multiplied with some time-dependent amplitude. The spatial basis functions can be local, such as hats, or global such as the sine basis functions shown earlier. This thesis will only focus on the class of methods involving global basis functions, known as spectral or modal methods [37].

Specifically, this thesis will make use of the eigenvalue expansion, wherein a set of eigenfunctions of the stationary problem is computed using, e.g., the power iteration method. For further details on this method, see, e.g., [38]. These eigenfunctions serve as basis functions for the problem. By this procedure, the initial partial differential equations are transformed into a set of coupled ordinary differential equations. The time-dependent amplitudes can then be found either by approximating an analytical form or by solving the system of equations numerically.

Figure 1.5: Thompson's tide predicting machine at the Science Museum, South Kensington, London [36]

1.5 Reduced Order Modelling Applied to Xenon Oscillation

A similar method to the one mentioned above was used by Christie and Poncelet [28] and John C. Lee [11] to find a solution to the xenon-iodine dynamics for a one-dimensional one-group reactor system with control rod movement but only includeded the first axial overtone in the analysis. Lee treated the axial oscillations separately from the diametral/azimuthal oscillations. Later in this thesis, it will be shown that the eigenfunctions of the axial dimensional problem are the sine series while the eigenfunctions of the diametral/azimuthal problem are the Bessel functions of the first kind multiplied with a sine series.

Song and Cho [10] expressed the problem in terms of axial differences and used the Laplace transform to create an analytical expression for a two-group one-dimensional two-point reactor system in a paper from 1997. Later, in 1999, Song and Cho [39] used the Fourier expansion on the distributions of flux, iodine and xenon concentrations to eliminate the non-linearities arising from the inclusion of control rod movements. The same axial difference parameters and Laplace transform were employed in their 1999 paper as in their 1997 paper. Both papers by Song and Cho showed good agreement with high-fidelity numerical simulations.

1.6 Goal of the research

To assist in evaluating the extent to which the Swedish nuclear reactors can operate in load-follow conditions, this research aims at developing computationally efficient and physics-transparent models for predicting when a particular reactor configuration is stable or unstable with respect to xenon oscillations. In this thesis, two similar models have been developed using intrusive reduced order modelling. These models differ in the spatial and energy refinement. The effect of this refinement is investigated in the thesis. A stability prediction model needs to be sufficiently complex to accurately predict the phenomenon. Complexity often comes with some cost to transparency. A sufficiently transparent model might enable stability indicators to be derived for the Swedish reactors. By utilising an exceedingly complex model at the cost of transparency, this opportunity would be lost. The research currently focuses on the stability of Pressurised Water Reactors (PWRs) but could be extended to Boiling Water Reactors (BWRs). This research aims to provide valuable insights into the stability of Swedish nuclear reactors operating in load-following conditions. By comparing different modelling approaches and assessing their computational efficiency, accuracy, and transparency, this study seeks to contribute to the understanding of reactor stability.

1.7 Structure of the Thesis

Chapters 2 and 3 of this thesis present the two reduced order models that were developed during the PhD work to predict free-running xenon oscillations and that were published in

conference proceedings (see papers I and II). Chapter 4 discusses the results of the comparison between the two models. Chapter 5 provides conclusions and the outlook for the future work planned in the continuation of the PhD research.

2

Two-Group Heterogeneous Model

This chapter will present the mathematical derivation of the two-group heterogeneous ROM (2G-HET). The chapter will first provide some reasoning for the choice of method. Next, the mathematics and details of the method are explained and lastly, the parameters in the model are given.

2.1 Motivation for the Model Choice

The mathematical model presented in this chapter builds upon the spectral methods discussed in the previous chapter, as well as neutron diffusion theory. It incorporates the interactions between the two-group neutron flux and the concentrations of iodine-135, and xenon-135. By using an eigenmode expansion, four partial differential equations (PDEs) are transformed into a set of coupled ordinary differential equations (ODEs). The spatial eigenmodes are completely stationary and only their relative amplitudes change in time as opposed to nodal solvers where the flux for each spatial node is recalculated at each time step. Numerically solving the coupled ODEs describing the amplitudes gives a complete approximate description of the temporal and three-dimensional spatial variations of neutron flux, I-135 and Xe-135 concentrations within the reactor core.

Several industry-standard full-core neutronic solvers for PWR systems employ a two-group diffusion treatment with nodal resolution. In this nodal discretisation approach, the reactor core is divided into cuboids, whose properties are homogenized. The advantage of choosing a two-group heterogeneous treatment is that it can conveniently take input and produce output in a format that is compatible with the nodal discretisation scheme commonly used in industry solvers. Using a heterogeneous model allows for investigating core configurations at different burnup levels which can alter the axial power profiles as can be seen in Fig. 1.4.

When examining Fig. 1.3, it becomes apparent that the absorption cross section of xenon-135 is primarily significant at low neutron energies. To effectively analyse xenon oscillations within the core, a two-group treatment can be employed, which separates the neutron flux into two components: one thermal that is sensitive to xenon oscillations and another fast that is not.

2.2 Underlying Theory Behind the Model

2.2.1 The Stationary Problem

This section will introduce the equilibrium form of the governing equations. From this, valuable relations can be derived such as the equilibrium iodine and xenon concentrations as well as the orthogonality properties of the system.

The balance equation without time dependency for the two-group neutron flux, iodine-135 and xenon-135 concentrations can be written in compact form as:

$$-[\nabla \cdot \mathbf{D}(\mathbf{r})\nabla + \mathbf{\Sigma}(\mathbf{r})] \times \hat{\Phi}_{eq}(\mathbf{r}) + \frac{1}{k_{eff}}\mathbf{F}(\mathbf{r}) \times \hat{\Phi}_{eq}(\mathbf{r}) = 0 \tag{2.1}$$

$$\frac{1}{k_{eff}}\mathbf{\Gamma_I}(\mathbf{r}) \times \hat{\Phi}_{eq}(\mathbf{r}) - \hat{\mathbf{X}}\lambda_I(\mathbf{r})I_{eq}(\mathbf{r}) = 0 \tag{2.2}$$

$$\hat{\mathbf{X}}\lambda_I(\mathbf{r})I_{eq}(\mathbf{r}) + \frac{1}{k_{eff}}\mathbf{\Gamma_X}(\mathbf{r}) \times \hat{\Phi}_{eq}(\mathbf{r}) - \hat{\mathbf{X}}\lambda_X(\mathbf{r})X_{eq}(\mathbf{r}) - \overline{\mathbf{X}}\sigma_{ax}(\mathbf{r})X_{eq}(\mathbf{r}) \times \hat{\Phi}_{eq}(\mathbf{r}) = 0 \tag{2.3}$$

Where $I_{eq}(\mathbf{r})$ and $X_{eq}(\mathbf{r})$ are the equilibrium iodine and xenon concentrations respectively, $\sigma_{a,x}(\mathbf{r})$ is the microscopic neutron absorption cross section for xenon-135 for thermal neutrons. The definitions of the different parameters can be found in A.

The vector $\hat{\mathbf{X}}$ has the property:

$$\hat{\mathbf{X}}^T \cdot \hat{\mathbf{X}} = 1 \tag{2.4}$$

Equations (2.1) to (2.3) are written in a general heterogeneous way.

The adjoint diffusion problem for the neutron equilibrium neutron population can be written as:

$$[\nabla \cdot \mathbf{D}(\mathbf{r})\nabla + \mathbf{\Sigma}^T(\mathbf{r})] \times \hat{\Phi}_{eq}^\dagger(\mathbf{r}) = \frac{1}{k_{eff}^\dagger}\mathbf{F}(\mathbf{r}) \times \hat{\Phi}_{eq}^\dagger(\mathbf{r}) \tag{2.5}$$

The adjoint neutron flux satisfies the relation:

$$\left\langle \hat{\Phi}^\dagger(\mathbf{r}) \middle| \mathbf{A}(\mathbf{r}) \times \hat{\Phi}(\mathbf{r}) \right\rangle = \left\langle \mathbf{A}^\dagger(\mathbf{r}) \times \hat{\Phi}^\dagger(\mathbf{r}) \middle| \hat{\Phi}(\mathbf{r}) \right\rangle \tag{2.6}$$

With $A^\dagger$ being the adjoint operator to the operator A. with the inner product defined as

$$\left\langle \hat{\Psi}(\mathbf{r}) \middle| \hat{\Phi}(\mathbf{r}) \right\rangle = \int_V \hat{\Psi}(\mathbf{r}) \cdot \hat{\Phi}(\mathbf{r}) dV' = \int_V (\psi_1(\mathbf{r})\phi_1(\mathbf{r}) + \psi_2(\mathbf{r})\phi_2(\mathbf{r})) dV' \tag{2.7}$$

From Eq. (2.2) and Eq. (2.3) the equilibrium iodine and xenon concentrations can be derived as

$$I_{eq}(\mathbf{r}) = \hat{\mathbf{X}}^T \cdot \frac{1}{k_{eff}\lambda_I(\mathbf{r})} \mathbf{\Gamma_I}(\mathbf{r}) \times \hat{\Phi}_{eq}(\mathbf{r}) \tag{2.8}$$

$$X_{eq}(\mathbf{r}) = \frac{\lambda_I(\mathbf{r})I_{eq}(\mathbf{r}) + \hat{\mathbf{X}}^T \cdot \frac{1}{k_{eff}} \mathbf{\Gamma_X}(\mathbf{r}) \times \hat{\Phi}_{eq}(\mathbf{r})}{\lambda_X(\mathbf{r}) + \hat{\mathbf{X}}^T \times \overline{\mathbf{X}} \cdot \sigma_{a,X}(\mathbf{r})\hat{\Phi}_{eq}(\mathbf{r})} \tag{2.9}$$

where Eq. (2.3) is multiplied by $\hat{\mathbf{X}}^T$ from the left and the property of Eq. (2.4) is used.

The forward problem is an eigenvalue problem with infinitely many solutions to the eigenvalue and the eigenvectors which satisfy the equation:

$$[\nabla \cdot \mathbf{D}(\mathbf{r})\nabla + \mathbf{\Sigma}(\mathbf{r})] \times \hat{\Phi}_n(\mathbf{r}) = \frac{1}{k_n}\mathbf{F}(\mathbf{r}) \times \hat{\Phi}_n(\mathbf{r}) \tag{2.10}$$

Here, $k_0 = k_{eff}$ and the spatial eigenmodes $\hat{\Phi}_n(\mathbf{r})$ are ordered with decreasing corresponding eigenvalues, such that $k_0 > k_1 > k_2....$

Importantly, it has been shown that the following orthogonality relation holds [11]:

$$\left\langle \hat{\Phi}_n^\dagger(\mathbf{r}) \middle| \mathbf{F}(\mathbf{r}) \times \hat{\Phi}_m(\mathbf{r}) \right\rangle = \left\langle \mathbf{F}^T(\mathbf{r}) \times \hat{\Phi}_n^\dagger(\mathbf{r}) \middle| \hat{\Phi}_m(\mathbf{r}) \right\rangle = \delta_{nm} \left\langle \hat{\Phi}_n^\dagger(\mathbf{r}) \middle| \mathbf{F}(\mathbf{r}) \times \hat{\Phi}_m(\mathbf{r}) \right\rangle \tag{2.11}$$

2.2.2 The Dynamic Problem

The definitions derived in the previous section are applied to a time-dependent problem in order to simplify it and develop a reduced order model.

The time-dependent problem is written as:

$$\mathbf{v}^{-1}\frac{\partial \hat{\Phi}(\mathbf{r}, t)}{\partial t} = \left[-\nabla \cdot \mathbf{D}(\mathbf{r})\nabla - \Sigma^{wox}(\mathbf{r}) - \tilde{\mathbf{X}}\sigma_{ax}X(\mathbf{r}, t) + \frac{1}{k_{eff}}\mathbf{F}(\mathbf{r}) \right] \times \hat{\Phi}(\mathbf{r}, t) \tag{2.12}$$

$$- \frac{\partial \Sigma_a}{\partial \hat{\Phi}}(\mathbf{r})\mathbf{\Phi}_{eq}(\mathbf{r}) \times \delta\hat{\Phi}(\mathbf{r}, t)$$

$$\hat{\mathbf{X}}\frac{\partial I(\mathbf{r}, t)}{\partial t} = \frac{1}{k_{eff}}\mathbf{\Gamma_I}(\mathbf{r}) \times \hat{\Phi}(\mathbf{r}, t) - \hat{\mathbf{X}}\lambda_I(\mathbf{r})I(\mathbf{r}, t) \tag{2.13}$$

$$\hat{\mathbf{X}}\frac{\partial X(\mathbf{r}, t)}{\partial t} = \hat{\mathbf{X}}\lambda_I(\mathbf{r})I(\mathbf{r}, t) + \frac{1}{k_{eff}}\mathbf{\Gamma_X}(\mathbf{r}) \times \hat{\Phi}(\mathbf{r}, t) \tag{2.14}$$

$$- \hat{\mathbf{X}}\lambda_X(\mathbf{r})X(\mathbf{r}, t) - \overline{\mathbf{X}}\sigma_{ax}X(\mathbf{r}, t) \times \hat{\Phi}(\mathbf{r}, t)$$

17

It can be assumed that the changes in the cross sections from power oscillations can be modelled through changes in the xenon concentration and the linear feedback term $-\frac{\partial \Sigma_a}{\partial \hat{\Phi}}(\mathbf{r})\mathbf{\Phi}_{eq}(\mathbf{r}) \times \delta\hat{\Phi}(\mathbf{r},t)$ with $\mathbf{\Phi}_{eq}(\mathbf{r})$ being a matrix with the equilibrium fast and thermal fluxes on the diagonal.

The two-group neutron flux, iodine concentration and xenon concentration can be written as a sum between the steady-state value and a time-dependent perturbation in the following manner.

$$\hat{\Phi}(\mathbf{r},t) = \hat{\Phi}_{eq}(\mathbf{r}) + \delta\hat{\Phi}(\mathbf{r},t) \tag{2.15}$$

$$I(\mathbf{r},t) = I_{eq}(\mathbf{r}) + \delta I(\mathbf{r},t) \tag{2.16}$$

$$X(\mathbf{r},t) = X_{eq}(\mathbf{r}) + \delta X(\mathbf{r},t) \tag{2.17}$$

The following steps are taken: equations (2.15) to (2.17) are inserted into Eqs. (2.12) to (2.14) and the stationary problem in Eqs. (2.1) to (2.3) are subtracted. Lastly, the equations are linearised by neglecting terms of the order δ^2. The result is balance equations for the changes around the mean of the variables of interest:

$$\mathbf{v}^{-1}\frac{\partial\delta\hat{\Phi}(\mathbf{r},t)}{\partial t} = \left[-\nabla\cdot\mathbf{D}(\mathbf{r})\nabla - \mathbf{\Sigma}(\mathbf{r}) - \frac{\partial\Sigma_a}{\partial\hat{\Phi}}(\mathbf{r})\mathbf{\Phi}_{eq}(\mathbf{r}) + \frac{1}{k_{eff}}\mathbf{F}(\mathbf{r})\right] \times \delta\hat{\Phi}(\mathbf{r},t) \tag{2.18}$$

$$- \left(\tilde{\mathbf{X}} \times \sigma_{ax}\hat{\Phi}_{eq}(\mathbf{r}) \otimes \hat{\mathbf{X}}^T\right) \times \hat{\mathbf{X}}\delta X(\mathbf{r},t)$$

$$\hat{\mathbf{X}}\frac{\partial\delta I(\mathbf{r},t)}{\partial t} = \frac{1}{k_{eff}}\mathbf{\Gamma_I}(\mathbf{r}) \times \delta\hat{\Phi}(\mathbf{r},t) - \hat{\mathbf{X}}\lambda_I(\mathbf{r})\delta I(\mathbf{r},t) \tag{2.19}$$

$$\hat{\mathbf{X}}\frac{\partial\delta X(\mathbf{r},t)}{\partial t} = \hat{\mathbf{X}}\lambda_I(\mathbf{r})\delta I(\mathbf{r},t) + \left[\frac{1}{k_{eff}}\mathbf{\Gamma_X}(\mathbf{r}) - \overline{\mathbf{X}}\sigma_{ax}X_{eq}(\mathbf{r})\right] \times \delta\hat{\Phi}(\mathbf{r},t) \tag{2.20}$$

$$- [\lambda_X(\mathbf{r}) + \overline{\mathbf{X}} \times \sigma_{a,X}(\mathbf{r})\hat{\Phi}_{eq}(\mathbf{r}) \otimes \hat{\mathbf{X}}^T] \times \hat{\mathbf{X}}\delta X(\mathbf{r},t)$$

The last terms of Eq. (2.18) and Eq. (2.20) are rewritten using the property in Eq. (2.4) and the $\otimes$ denote the outer product between two vectors such that:

$$\hat{v} \otimes \hat{w}^T = \begin{bmatrix} v_1 \\ v_2 \\ \vdots \\ v_n \end{bmatrix} \otimes \begin{bmatrix} w_1 \\ w_2 \\ \vdots \\ w_m \end{bmatrix}^T = \begin{bmatrix} v_1w_1 & v_1w_2 & \cdots & v_1w_m \\ v_2w_1 & v_2w_2 & \cdots & v_2w_m \\ \vdots & \vdots & \ddots & \vdots \\ v_nw_1 & v_nw_2 & \cdots & v_nw_m \end{bmatrix} \tag{2.21}$$

The truncated eigenmode expansion is applied to approximate $\delta\hat{\Phi}$, δI and δX with a separation of the perturbation into time-dependent amplitudes and use the space-dependent eigenfunctions of the forward problem as basis functions.

$$\delta\hat{\Phi}(\mathbf{r}, t) \approx \sum_{n=0}^{N} P_n(t)\hat{\Phi}_n(\mathbf{r}) \tag{2.22}$$

$$\hat{\mathbf{X}}\delta I(\mathbf{r}, t) \approx \sum_{n=0}^{N} A_n\mathbf{F}(\mathbf{r})I_n(t) \times \hat{\Phi}_n(\mathbf{r}) \tag{2.23}$$

$$\hat{\mathbf{X}}\delta X(\mathbf{r}, t) \approx \sum_{n=0}^{N} A_n\mathbf{F}(\mathbf{r})X_n(t) \times \hat{\Phi}_n(\mathbf{r}) \tag{2.24}$$

where $A_n = \frac{\langle\hat{\Phi}_n^\dagger(\mathbf{r})|\hat{\Phi}_n(\mathbf{r})\rangle}{\langle\hat{\Phi}_n^\dagger(\mathbf{r})|\mathbf{F}(\mathbf{r})\times\hat{\Phi}_n(\mathbf{r})\rangle}$ transforms the units into $[cm^{-3}]$. By multiplying by the adjoint flux and integrating over the volume of the reactor, the partial differential equations are now transformed into a set of $3N$ ordinary differential equations.

$$\frac{\mathrm{d}P_m(t)}{\mathrm{d}t} = \frac{1}{\Lambda_m}\left(\frac{1}{k_0} - \frac{1}{k_m}\right)P_m(t) - \frac{\partial\Sigma_a}{\partial\hat{\Phi}}\sum_{n=0}^{N}\frac{\langle\hat{\Phi}_m^\dagger(\mathbf{r})|\mathbf{\Phi}_{eq}(\mathbf{r})\times\hat{\Phi}_n(\mathbf{r})\rangle}{\langle\hat{\Phi}_m^\dagger(\mathbf{r})|\mathbf{v}^{-1}\times\hat{\Phi}_m(\mathbf{r})\rangle}P_n(t) \tag{2.25}$$

$$- \frac{1}{\Lambda_m}\sum_{n=0}^{N}\frac{\langle\hat{\Phi}_m^\dagger(\mathbf{r})|\sigma_{a,X}(\mathbf{r})\left(\tilde{\mathbf{X}}\times\mathbf{\Phi}_{eq}(\mathbf{r})\right)\times\mathbf{F}(\mathbf{r})\times\hat{\Phi}_n(\mathbf{r})\rangle}{\langle\hat{\Phi}_m^\dagger(\mathbf{r})|\mathbf{F}(\mathbf{r})\times\hat{\Phi}_m(\mathbf{r})\rangle}A_nX_n(t)$$

$$\frac{\mathrm{d}I_m(t)}{\mathrm{d}t} = \frac{1}{A_mk_0}\frac{\langle\hat{\Phi}_m^\dagger(\mathbf{r})|\mathbf{\Gamma_I}(\mathbf{r})\times\hat{\Phi}_m(\mathbf{r})\rangle}{\langle\hat{\Phi}_m^\dagger(\mathbf{r})|\mathbf{F}(\mathbf{r})\times\hat{\Phi}_m(\mathbf{r})\rangle}P_m(t) - \lambda_I I_m(t) \tag{2.26}$$

$$\frac{\mathrm{d}X_m(t)}{\mathrm{d}t} = \lambda_I I_m(t) + \frac{1}{A_mk_0}\frac{\langle\hat{\Phi}_m^\dagger(\mathbf{r})|\mathbf{\Gamma_X}(\mathbf{r})\times\mathbf{\Phi}_m(\mathbf{r})\rangle}{\langle\hat{\Phi}_m^\dagger(\mathbf{r})|\mathbf{F}(\mathbf{r})\times\hat{\Phi}_m(\mathbf{r})\rangle}P_m(t) \tag{2.27}$$

$$- \frac{1}{A_m}\sum_{n=0}^{N}\frac{\langle\hat{\Phi}_m^\dagger(\mathbf{r})|\sigma_{a,x}(\mathbf{r})\overline{\mathbf{X}}X_{eq}(\mathbf{r})\times\hat{\Phi}_n(\mathbf{r})\rangle}{\langle\hat{\Phi}_m^\dagger(\mathbf{r})|\mathbf{F}(\mathbf{r})\times\hat{\Phi}_m(\mathbf{r})\rangle}P_n(t)$$

$$- \lambda_X X_m(t) - \sum_{n=0}^{N}\frac{\langle\hat{\Phi}_m^\dagger(\mathbf{r})|\left(\sigma_{a,X}(\mathbf{r})\overline{\mathbf{X}}\times\mathbf{\Phi}_{eq}(\mathbf{r})\right)\times\mathbf{F}(\mathbf{r})\times\hat{\Phi}_n(\mathbf{r})\rangle}{\langle\hat{\Phi}_m^\dagger(\mathbf{r})|\mathbf{F}(\mathbf{r})\times\hat{\Phi}_m(\mathbf{r})\rangle}\frac{A_n}{A_m}X_n(t)$$

Where, $\Lambda_{n,m} = \frac{\langle\hat{\Phi}_m^\dagger(\mathbf{r})|\mathbf{v}^{-1}\times\hat{\Phi}_n(\mathbf{r})\rangle}{\langle\hat{\Phi}_m^\dagger(\mathbf{r})|\mathbf{F}(\mathbf{r})\times\hat{\Phi}_m(\mathbf{r})\rangle}$ and it was assumed that $\Lambda_{n,m} << \Lambda_{m,m}$ for $n \neq m$.

In the ODEs presented above, mode m is coupled with all other modes n through the sums of inner products.

The model's results will be shown and compared with those from the one-group homogeneous model (1G-HOM) in Chapter 4. The normalised neutron flux profiles, resulting from the given cross sections, of the core can be seen in Fig. 2.1
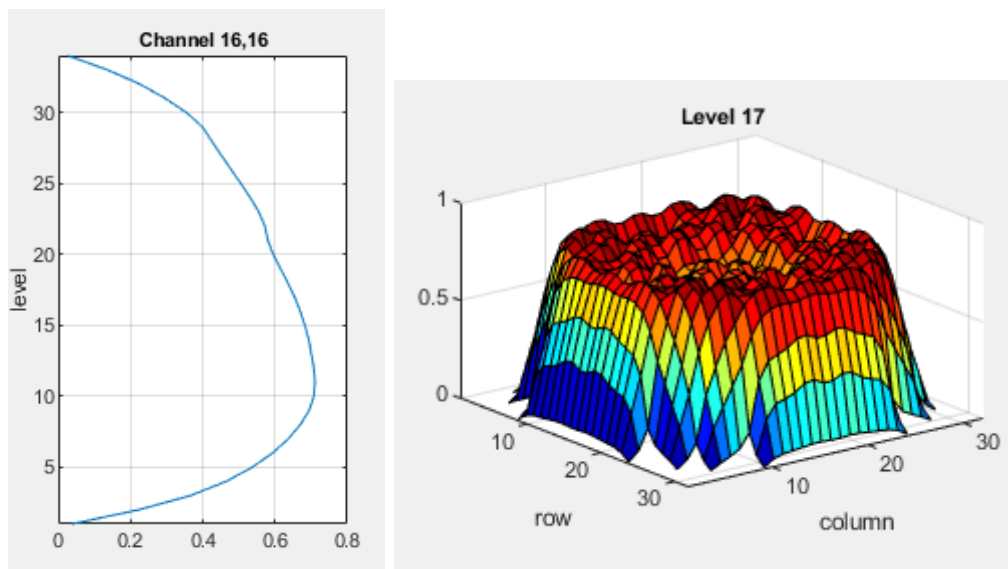
Figure 2.1: Axial (left) and radial (right) normalised neutron flux profile in nodal dimensions

3

One-Group Homogenous Model

In the previous chapter, the two-group heterogeneous formulation of the reduced order model was introduced, highlighting the compatibility with industry-standard full-core solvers and its ability to capture the xenon-neutron interactions more accurately due to the increased energy resolution. However, there are distinct advantages to employing a simpler one-group homogeneous treatment. This approach facilitates a deeper understanding of the underlying physics governing the system dynamics. Additionally, it enables the derivation of a fully analytical expression for the system evolution.

This chapter will first present the derivation of the one-group homogeneous model. Next, it will go through the derivation of the three-dimensional eigenfunctions of the one-group homogeneous diffusion equations in cylindrical coordinates. Lastly, the analytical derivation of the complex stability index, which solely describes the dynamics of the model, is presented.

3.1 Underlying Theory of the Model

The derivation of the 1G-HOM model follows the same approach as the 2G-HET model. First, the equilibrium equations are presented along with the equilibrium concentrations of xenon-135 and iodine-135 and the orthogonality properties.

3.1.1 The Stationary Problem

The one-group diffusion equation with homogenised cross sections looks as follows:

$$D\nabla^2\phi_{eq}(\mathbf{r}) + \left[\tfrac{1}{k_{eff}}\nu\Sigma_f - \Sigma_a\right]\phi_{eq}(\mathbf{r}) = 0 \tag{3.1}$$

$$\frac{\gamma_I}{k_{eff}}\Sigma_f\phi_{eq}(\mathbf{r}) - \lambda_I I_{eq}(\mathbf{r}) = 0 \tag{3.2}$$

$$\lambda_I I_{eq}(\mathbf{r}) + \frac{\gamma_X}{k_{eff}}\Sigma_f\phi_{eq}(\mathbf{r}) - \lambda_X X_{eq}(\mathbf{r}) - \sigma_X\phi_{eq}(\mathbf{r})X_{eq}(\mathbf{r}) = 0 \tag{3.3}$$

These functions are greatly simplified compared to the heterogeneous equations since none of the cross sections carry spatial dependence.

The equilibrium concentrations of iodine and xenon are given in Eqs. (1.1) and (1.2).

Again, this diffusion equation is an eigenvalue equation with infinite solutions satisfying:

$$D\nabla^2\phi_n(\mathbf{r}) + \left[\tfrac{1}{k_n}\nu\Sigma_f - \Sigma_{a,w/oX}(\mathbf{r}) - X_{eq}(\mathbf{r})\sigma_X\right]\phi_n(\mathbf{r}) = 0 \tag{3.4}$$

With the following orthogonality property

$$\int_V \phi_m(\mathbf{r})\phi_n(\mathbf{r})dV = \delta_{nm}\int_V \phi_m(\mathbf{r})\phi_n(\mathbf{r})dV \tag{3.5}$$

3.1.2 The Dynamic Problem

In the one-group homogeneous formalism, the time-dependent equations are written as:

$$\frac{1}{v}\frac{\partial\phi(\mathbf{r},t)}{\partial t} = D\nabla^2\phi(\mathbf{r},t) + \left[\tfrac{1}{k_{eff}}\nu\Sigma_f - \Sigma_{a,w/oX}(\mathbf{r}) - X(\mathbf{r},t)\sigma_X\right]\phi(\mathbf{r},t) \tag{3.6}$$

$$\frac{\partial I(\mathbf{r},t)}{\partial t} = \frac{\gamma_I}{k_{eff}}\Sigma_f\phi(\mathbf{r},t) - \lambda_I I(\mathbf{r},t) \tag{3.7}$$

$$\frac{\partial X(\mathbf{r},t)}{\partial t} = \lambda_I I(\mathbf{r},t) + \frac{\gamma_X}{k_{eff}}\Sigma_f\phi(\mathbf{r},t) - \lambda_X X(\mathbf{r},t) - \sigma_{aX}\phi(\mathbf{r},t)X(\mathbf{r},t) \tag{3.8}$$

Again, the non-linear coupling between the neutron flux and xenon concentrations can be seen in Eqs. (3.6) and (3.8).

As in the 2G-HET model, the time-dependent variations are separated from the static spatial distributions. The static parts are then subtracted from the dynamic equations and the terms of order δ^2 are neglected to yield the balance equations for the changes around the mean value of the variables of interest.

$$\frac{1}{v}\frac{\partial\delta\phi(\mathbf{r},t)}{\partial t} = D\nabla^2\delta\phi(\mathbf{r},t) + \Sigma_E\delta\phi(\mathbf{r},t) - \sigma_X\phi_{eq}(\mathbf{r})\delta X(\mathbf{r},t) - \frac{\partial\Sigma_a}{\partial\phi}\phi_{eq}(\mathbf{r})\delta\phi(\mathbf{r},t) \tag{3.9}$$

$$\frac{\partial\delta I(\mathbf{r},t)}{\partial t} = \frac{\gamma_I}{k_{eff}}\Sigma_f\delta\phi(\mathbf{r},t) - \lambda_I\delta I(\mathbf{r},t) \tag{3.10}$$

$$\begin{aligned}\frac{\partial\delta X(\mathbf{r},t)}{\partial t} = {} & \lambda_I\delta I(\mathbf{r},t) + \frac{\gamma_X}{k_{eff}}\Sigma_f\delta\phi(\mathbf{r},t) - \lambda_X\delta X(\mathbf{r},t)\\ & - \sigma_X\phi_{eq}(\mathbf{r})\delta X(\mathbf{r},t) - \sigma_X X_{eq}(\mathbf{r})\delta\phi(\mathbf{r},t)\end{aligned} \tag{3.11}$$

Using the definition $\Sigma_E = \frac{\nu\Sigma_f}{k_{eff}} - \Sigma_a$.

The three variables are expanded in the spatial eigenmodes of the system multiplied with a time-dependent amplitude:

$$\delta\phi(\mathbf{r}, t) \approx \sum_{n=0}^{N} P_n(t)\Phi_n(\mathbf{r}) \tag{3.12}$$

$$\delta I(\mathbf{r}, t) \approx \sum_{n=0}^{N} I_n(t)\Phi_n(\mathbf{r}) \tag{3.13}$$

$$\delta X(\mathbf{r}, t) \approx \sum_{n=0}^{N} X_n(t)\Phi_n(\mathbf{r}) \tag{3.14}$$

In the above approximation, the solution becomes exact in the limit $N \to \infty$.

The Helmholtz equation $\nabla^2\Phi_n(r) = -B_n^2\Phi_n(r)$ is applied and the mode $\Phi_m(r)$ is multiplied from the left. Then, all terms are integrated over the volume of the reactor, making use of the orthogonal relationship between the modes:

$$\int_V \Phi_m(r)\Phi_n(r)dV = \delta_{nm}\int_V \Phi_m(r)\Phi_n(r)dV \tag{3.15}$$

The expressions for the time-dependence of the amplitudes then become:

$$\frac{1}{v}\frac{dP_m(t)}{dt} = (-DB_m^2 + \Sigma_E)P_m(t) - \sigma_X\sum_n^N \Phi_0^{m,n}X_n(t) - \frac{\partial\Sigma_a}{\partial\phi}\sum_n^N \Phi_0^{m,n}P_n(t) \tag{3.16}$$

$$\frac{dI_m(t)}{dt} = \gamma_I\frac{\Sigma_f}{k_{eff}}P_m(t) - \lambda_I I_m(t) \tag{3.17}$$

$$\frac{dX_m(t)}{dt} = \lambda_I I_m(t) + \frac{\gamma_X}{k_{eff}}\Sigma_f P_m(t) - \sigma_X\sum_n^N X_0^{m,n}P_n(t) \tag{3.18}$$

$$- \lambda_X X_m(t) - \sigma_X\sum_n^N \Phi_0^{m,n}X_n(t)$$

Where $\Phi_0^{mn} = \dfrac{\int_V \phi_{eq}(r)\Phi_m(r)\Phi_n(r)dV}{\int_V \Phi_m(r)^2 dV}$ and $X_0^{mn} = \dfrac{\int_V X_{eq}(r)\Phi_m(r)\Phi_n(r)dV}{\int_V \Phi_m(r)^2 dV}$ are the terms that couple one mode m to all other modes n.

The set of partial differential equations has now been transformed into a set of $3N$ coupled differential equations. The next section will go through the analytical derivation of the spatial eigenmodes of the three-dimensional one-group system.

A comparison of the 1G-HOM model and the 2G-HET model outputs of the time-dependent functions $P(t)$, $I(t)$ and $X(t)$ can be found in Section 4.4.

23

3.2 Calculating the Spatial Eigenmodes of the Homogenised System

The diffusion approximation is used for the case of a one-group 3-dimensional homogeneous reactor system assumed to be a perfect cylinder. The radius was calculated such that it preserved the area of the nodal reactor model.

Assuming a finite cylinder, with the origin in the middle, and having height H and radius P. The stationary homogeneous diffusion equation can be written in the form of a Helmholtz equation:

$$\nabla^2 \Phi(\rho, \theta, z) + B^2 \Phi(\rho, \theta, z) = 0 \tag{3.19}$$

Where ρ, θ and z denotes the radial, angular and the axial coordinate respectively.

Inserting the definition of the Laplacian in cylindrical coordinates one obtains:

$$\frac{1}{\rho}\frac{\partial}{\partial \rho}\left(\rho \frac{\partial \Phi(\rho, \theta, z)}{\partial \rho}\right) + \frac{1}{\rho^2}\frac{\partial^2 \Phi(\rho, \theta, z)}{\partial \theta^2} + \frac{\partial^2 \Phi(\rho, \theta, z)}{\partial z^2} + B^2 \Phi(\rho, \theta, z) = 0 \tag{3.20}$$

By applying the separation of variables it is possible to write the solution as:

$$\Phi(\rho, \theta, z) = R(\rho)\Theta(\theta)Z(z) \tag{3.21}$$

The following boundary conditions are imposed on the above functions:

$$R(P) = 0 \tag{3.22}$$
$$Z(\pm H/2) = 0 \tag{3.23}$$
$$\Theta(0) = \Theta(2\pi) \tag{3.24}$$

Where the extrapolation distance has been neglected. Inserting Eq. (3.21) into Eq. (3.20) and dividing by $R(\rho)\Theta(\theta)Z(z)$ the following expression is obtained:

$$\frac{1}{\rho}\left(\frac{(\rho R')'}{R}\right) + \frac{1}{\rho^2}\frac{\Theta''}{\Theta} + \frac{Z''}{Z} + B^2 = 0 \tag{3.25}$$

$$\Rightarrow \frac{1}{\rho}\left(\frac{(\rho R')'}{R}\right) + \frac{1}{\rho^2}\frac{\Theta''}{\Theta} = -\frac{Z''}{Z} - B^2 \tag{3.26}$$

Since the two sides of the equation are equal and depend on different variables both sides must be equal to a constant $-a^2$. The axial function

$$Z'' = (a^2 - B^2)Z \tag{3.27}$$

$$\tag{3.28}$$

can be solved separately and it can be shown that the solution has the form:

$$Z = Ae^{i\sqrt{B^2-a^2}z} + Ce^{-i\sqrt{B^2-a^2}z} \tag{3.29}$$

$$= E\cos\left(\sqrt{B^2-a^2}z\right) + F\sin\left(\sqrt{B^2-a^2}z\right) \tag{3.30}$$

By imposing the axial boundary conditions given in Eq. (3.23) the final axial solutions become:

$$Z = A\cos\left((2n+1)\frac{\pi}{H}z\right) + F\sin\left(2(n+1)\frac{\pi}{H}z\right) \tag{3.31}$$

with $n = 0, 1, 2...$ For the azimuthal solutions, the left-hand side of Eq. (3.26) is rewritten as:

$$\rho\frac{(\rho R')'}{R} + a_n^2\rho^2 = \frac{\Theta''}{\Theta} \tag{3.32}$$

Again, the two sides of the equation must each be equal to a constant b^2, and it can be shown that the azimuthal solutions must have the following form:

$$\Theta'' = b^2\Theta \tag{3.33}$$

$$\Rightarrow \Theta = A'e^{ib\theta} + C'e^{-ib\theta} \tag{3.34}$$

$$= E'\cos(b\theta) + F'\sin(b\theta) \tag{3.35}$$

By imposing the boundary condition from Eq. (3.24) the final azimuthal solutions become:

$$\Theta = E'\cos(m\theta) + F'\sin(m\theta) \tag{3.36}$$

with $m = 0, 1, 2...$

For the radial solutions, the remaining left-hand side of Eq. (3.32) is rewritten as:

25

$$\rho\frac{(\rho R')'}{R} + a_{m,i}^2\rho^2 - m^2 = 0 \tag{3.37}$$

or $\tag{3.38}$

$$R'' + \frac{1}{\rho}R' + \left(a_{m,i}^2 - \frac{m^2}{\rho^2}\right)R = 0 \tag{3.39}$$

Making a change of variables: $\omega = a_{m,i}\rho$, and $\mathcal{R}(\omega) = R\left(\frac{\omega}{a_{m,i}}\right)$ one gets:

$$\frac{\mathrm{d}^2\mathcal{R}}{\mathrm{d}\omega^2} + \frac{1}{\omega}\frac{\mathrm{d}\mathcal{R}}{\mathrm{d}\omega} + \left(1 - \frac{m^2}{\omega^2}\right)\mathcal{R} = 0 \tag{3.40}$$

This is now the form of a Bessel equation which, when reinserting the original variables, has solutions on the form:

$$R = BJ_m(a_{m,i}\rho) + CY_m(a_{m,i}\rho) \tag{3.41}$$

Here, J_m and Y_m are Bessel functions of the first and second kind respectively with the order of the functions denoted by m.

Since $Y_m(x) \to -\infty$ as $x \to 0$, C must equal zero.

By imposing the boundary condition of Eq. (3.22) it follows that $a_{m,i} = j_{m,i}/P$ where $j_{m,i}$ is the i-th root of J_m.

The total geometrical buckling is defined as:

$$B_{n,m,i}^2 = \left(\frac{j_{m,i}}{P}\right)^2 + \left((2n+1)\frac{\pi}{H}\right)^2 \tag{3.42}$$

We define the axial buckling κ_n^2 and radial buckling $a_{m,i}^2$ respectively as:

$$\kappa_n^2 = \left((2n+1)\frac{\pi}{H}\right)^2 \tag{3.43}$$

$$a_{m.i}^2 = \left(\frac{j_{m,i}}{P}\right)^2 \tag{3.44}$$

Since both the axial and azimuthal dimensions have two solutions four combined solutions are obtained:

$$\Phi(\rho, \theta, z) = C J_m(a_{m,i}\rho) \cos(m\theta) \cos(\kappa_n z)$$
$$\Phi(\rho, \theta, z) = C J_m(a_{m,i}\rho) \sin(m\theta) \sin\left(\left(\kappa_n - \tfrac{\pi}{H}\right)z\right)$$
$$\Phi(\rho, \theta, z) = C J_m(a_{m,i}\rho) \cos(m\theta) \sin\left(\left(\kappa_n - \tfrac{\pi}{H}\right)z\right)$$
$$\Phi(\rho, \theta, z) = C J_m(a_{m,i}\rho) \sin(m\theta) \cos(\kappa_n z)$$

$$(3.45)$$

The corresponding eigenvalues can be found as

$$k_{n,m,i} = \frac{\frac{\nu\Sigma_f}{\Sigma_a}}{1 + L^2 B_{n,m,i}^2} \tag{3.46}$$

Where $L = \sqrt{\frac{D}{\Sigma_a}}$ is the diffusion length of the system. These eigenfunctions constitute a complete set, are global and satisfy the orthogonality property of Eq. (3.15) and thus make for suitable basis functions.

A comparison and discussion of the calculated eigenvalues and coupling coefficients of the two models is presented in Section 4.6.

3.3 Analytical Calculation of Stability Index

To derive an analytical expression for the stability coefficient, an exponential form of the time-dependent functions for each mode in Eqs. (3.16) to (3.18) is assumed and the coupling between modes where $n \neq m$ is neglected.

$$P_m(t) = a_m e^{\omega_m t} \tag{3.47}$$
$$I_m(t) = b_m e^{\omega_m t} \tag{3.48}$$
$$X_m(t) = c_m e^{\omega_m t} \tag{3.49}$$

When these assumptions are inserted back into Eqs. (3.16) to (3.18) one obtains:

$$0 = \left(-\tfrac{\omega_m}{v} - DB_m^2 + \Sigma_E - \tfrac{\partial\Sigma_a}{\partial\phi}\phi_0^m\right)a_m - \sigma_X\phi_0^m c_m \tag{3.50}$$

$$0 = \frac{\gamma_I}{k_{eff}}\Sigma_f a_m - (\omega_m + \lambda_I)b_m \tag{3.51}$$

$$0 = \left(\frac{\gamma_X}{k_{eff}}\Sigma_f - \sigma_X X_0^m\right)a_m + \lambda_I b_m - (\omega_m + \lambda_X + \sigma_X\phi_0^m)c_m \tag{3.52}$$

These equations can be written in the following matrix form:

$$
\begin{bmatrix}
\begin{pmatrix} -\frac{\omega_m}{v} - DB_m^2 + \Sigma_E \\ -\frac{\partial \Sigma_a}{\partial \phi} \phi_0^m \end{pmatrix} & 0 & -\sigma_X \phi_0^m \\
\frac{\gamma_I}{k_{eff}} \Sigma_f & -(\lambda_I + \omega_m) & 0 \\
\frac{\gamma_X}{k_{eff}} \Sigma_f - \sigma_X X_0^m & \lambda_I & -\begin{pmatrix} \omega_m + \lambda_X \\ +\sigma_X \phi_0^m \end{pmatrix}
\end{bmatrix}
\begin{bmatrix} a_m \\ b_m \\ c_m \end{bmatrix} = \begin{bmatrix} 0 \\ 0 \\ 0 \end{bmatrix}
\tag{3.53}
$$

The only non-trivial solution is found by solving for the ω_m that satisfies the determinant equation:

$$
\begin{vmatrix}
\begin{pmatrix} -\frac{\omega_m}{v} - DB_m^2 + \Sigma_E \\ -\frac{\partial \Sigma_a}{\partial \phi} \phi_0^m \end{pmatrix} & 0 & -\sigma_X \phi_0^m \\
\frac{\gamma_I}{k_{eff}} \Sigma_f & -(\lambda_I + \omega_m) & 0 \\
\frac{\gamma_X}{k_{eff}} \Sigma_f - \sigma_X X_0^m & \lambda_I & -\begin{pmatrix} \omega_m + \lambda_X \\ +\sigma_X \phi_0^m \end{pmatrix}
\end{vmatrix} = 0
\tag{3.54}
$$

This can be rewritten into the following third-order equation:

$$
\left(-\frac{\omega_m}{v} - DB_m^2 + \Sigma_E - \frac{\partial \Sigma_a}{\partial \phi} \phi_0^m \right) (\lambda_I + \omega_m)(\omega_m + \lambda_X + \sigma_X \phi_0^m)
$$
$$
= \sigma_X \phi_0^m \left(\frac{\gamma_I}{k_{eff}} \Sigma_f \lambda_I + (\lambda_I + \omega_m) \left(\frac{\gamma_X}{k_{eff}} \Sigma_f - \sigma_X X_0^m \right) \right)
\tag{3.55}
$$

From this, three complex roots of ω_m are found for each mode. From Eqs. (3.47) to (3.49) the following two conclusions can be drawn:

- If a root has a positive real value the corresponding mode will diverge over time with a doubling time dependent on the real value.

- If a root has a negative real value the corresponding mode will converge over time with a decay constant dependent on the real value.

- If a root has a non-zero imaginary value the corresponding mode will oscillate in time, with a frequency dependent on the imaginary value.

Such an understanding of the behaviour of isolated modes, without the effects of cross-mode coupling, gives insight into the underlying dynamics of the system modelled. Knowing which modes are unstable provides the possibility of assessing the individual sensitivity of that mode to reactor-specific parameters. The 1G-HOM model, through its simplicity, thus gives additional important information relevant to xenon oscillation control and avoidance strategies.

A comparison of the analytical results for the 1G-HOM and a similar analysis done with the 2G-HET model coefficients for the coupled ODEs is presented in Section 4.5. A sensitivity

analysis investigating the 1G-HOM model response to changes in the different reactor-specific parameters is presented in Section 4.3. This analysis is not included in the appended papers providing additional insights beyond the scope of the published research.

4

Results and Comparisons of the Models

The previous two chapters introduced and explained the 2G-HET and 1G-HOM models in detail. First, this chapter introduces the data used for the modelling along with the condensation and homogenisation schemes used to transform the data for the 1G-HOM model. Then, the chapter presents a novel sensitivity analysis, based on the 1G-HOM model, that is not included in the appended papers. The objective of this analysis is to gain insight into the primary parameters affecting the stability of xenon oscillations. Then, the predictions of the modes' time-dependent behaviour are compared numerically and analytically between the two models. Next, the effects of eigenvalue separation, energy and spatial refinement are investigated to illuminate any underlying causes of differences between the two models.

4.1   Explanation of the Data Used

In the case study, the 2G-HET and 1G-HOM models are applied to analyse the case of an asymmetric axial perturbation in a typical western PWR core [40] that has a nominal power level of 3565 MWth and contains 193 fuel assemblies arranged in a 17x17 lattice.

The physical constants used in the model are tabulated in Table 4.1.

The cross section data has nodal dimensions of $X \times Y \times Z = 32 \times 32 \times 34$ and is prepared with a high degree of negative equilibrium axial offset $ESI = -20.5\%$, i.e., the power at equilibrium is 20.5% higher at the bottom of the core than at the top.

4.2   Condensation and Homogenisation of the Cross Sections

The 1G-HOM model is built upon the same data as the 2G-HET model. This nodal data in two energy groups is transformed into one energy group and homogenised over the entire reactor. By making a weighted average using the neutron flux as a weighting factor, the

Parameter	Value
λ_I	$2.87 \cdot 10^{-5}$ s^{-1}
λ_X	$2.09 \cdot 10^{-5}$ s^{-1}
γ_I	0.062
γ_X	0.002
σ_X	$2.70 \cdot 10^{-18}$ cm^2
ν	2.44
κ	$0.2976 \cdot 10^{-10}$ J
Radius	180.87 cm
Height	388.62 cm
Nominal power	$3.565 \cdot 10^9$ W
$\frac{\partial \Sigma_a}{\partial \tilde{\Phi}}$	$1.3 \cdot 10^{-18}$ cm s

Table 4.1: Physical constants and reactor specific parameters.

reaction rate is conserved. First, the energy condensation is written as:

$$\Sigma_{i,G,\alpha} = \frac{\sum_g \Sigma_{i,g,\alpha}\phi_{i,g}}{\sum_g \phi_{i,g}} \tag{4.1}$$

Where $g = 1, 2$ denotes the energy group and Σ_α is the cross section of the nuclear reaction in question and i denotes the node index.

Then, the data is subsequently homogenized by using the neutron flux as a weighting function. In the most general case, the equation is expressed as:

$$\Sigma_{I,G,\alpha} = \frac{\sum_i \Sigma_{i,G,\alpha}\phi_{i,G}V_i}{\sum_i \phi_{i,G}V_i} \tag{4.2}$$

However, in this particular scenario, all nodes are of the same size, rendering the node sizes V_i negligible. The condensed and homogenised flux are respectively defined as follows: $\phi_{i,G} = \sum_g \phi_{i,g}$ and $\phi_{I,G} = \sum_i \phi_{i,G}$.

Table 4.2 shows the homogenised and condensed cross sections used for the 1G-HOM model. It should be mentioned that in the condensation of the microscopic cross section of xenon-135, the fast cross section was neglected due to its much lower value as is evident from Fig. 1.3.

A comparative evaluation of the effects of condensation and homogenisation of the nodal input data on model prediction is presented in Sections 4.8 and 4.9 respectively.

| Parameter	Value
$\nu\Sigma_f$	$0.02976 \ \text{cm}^{-1}$
Σ_a	$0.0227 \ \text{cm}^{-1}$
D	$0.9846 \ \text{cm}^2 \ \text{s}^{-1}$
σ_X	$3.92 \cdot 10^{-19} \ \text{cm}^{-2}$
v	$1.51 \cdot 10^6 \ \text{cm} \ \text{s}^{-1}$

Table 4.2: Homogenised and condensed cross sections.

4.3 Sensitivity Analysis

Utilizing the 1G-HOM model allows for additional insights into the impact that each model parameter has on the time-dependent behaviour of any given mode. The analysis is carried out by systematically changing each of the following parameters: Height, radius, diffusion coefficient D, power level, macroscopic absorption cross-section Σ_a and the feedback coefficient $\frac{\partial \Sigma_a}{\partial \phi}$ then recalculating the roots of the stability coefficient ω_m using Eq. (3.55). Only the roots related to the iodine-xenon behaviour are shown as the one related to the prompt behaviour of the system is of limited relevance for this analysis. For all plots, the two roots are shown in red and blue respectively with the real value represented as a solid line and the imaginary value of each root as a dashed line. In the regime where the imaginary values are zero, the behaviour can be described as a sum of two exponential functions with the two real values being the respective exponential coefficients. When the imaginary values are non-zero, the real parts of the two roots overlap and only the blue line is visible. In this region, the amplitudes oscillate with a frequency corresponding to the imaginary values and increase or decrease exponentially with the real values being the exponential coefficient. For each parameter, 100 different values are considered, ranging from minimum to maximum values which were deemed relevant for each given parameter.

In the comparison between the models, the following naming convention is used:

- **Mode 1** is the fundamental mode having the same shape as the equilibrium neutron flux distribution.

- **Mode 2** has the first harmonic in the axial direction and the same shape as mode 1 in the radial plane.

- **Mode 3** has the second harmonic in the axial direction and the same shape as modes 1 and 2 in the radial plane.

The analysis can be carried out for all modes but for the sake of brevity, only the sensitivity of the first axial harmonic combined with the fundamental radial and azimuthal harmonics (mode 2) is shown in this thesis. The stability of the system can be tuned using the arbitrary
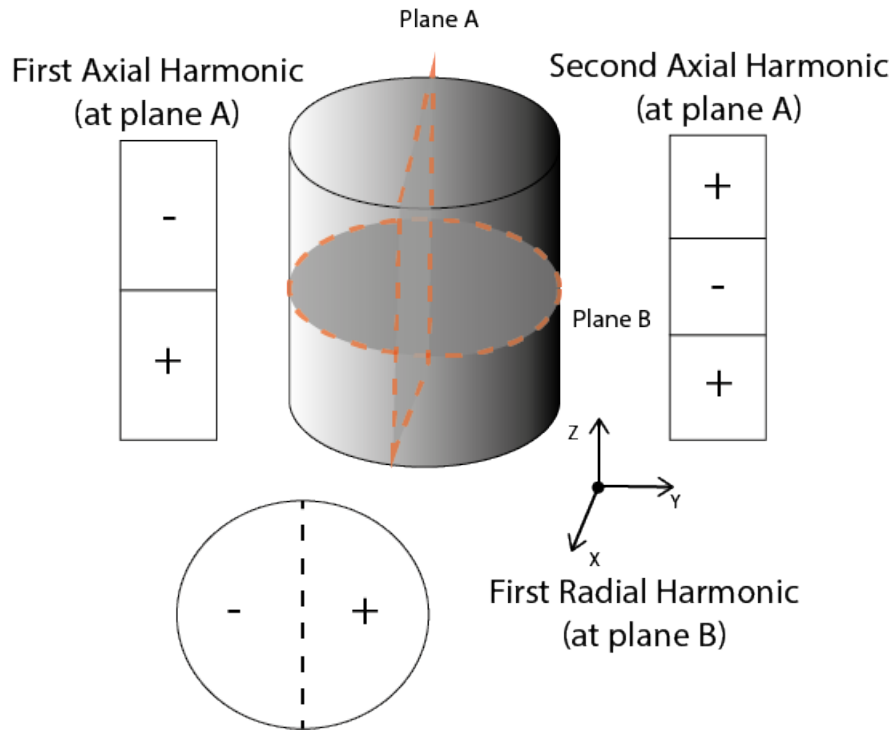
Figure 4.1: Schematics of the first and second harmonics of the system (inspired by [13])

value of $\frac{\partial \Sigma_a}{\partial \phi}$. Because of the large differences in stability between the two models, the value of $\frac{\partial \Sigma_a}{\partial \phi}$ is reduced by a factor of 10 compared to the value used in the remaining sections for both the 1G-HOM and 2G-HET models.

Fig. 4.1 illustrates the first axial and radial harmonics of the system.

4.3.1 Impact of Reactor Height and Radius

The dimensions of the system have an impact on several parameters. They affect the buckling $B_{n,m,i}$, resulting also in an effect on the effective multiplication factor. For this analysis, the neutron flux was kept constant such that the power of the system changed with the size. The changes in neutron flux affect both the terms ϕ_0^m and X_0^m as these are dependent on the equilibrium neutron flux. Additionally, any integral over the volume is affected by changes in the reactor dimensions.

Both the maximum and minimum height and radius variations were set to be 120% and 50% of the nominal values given in table Table 4.1, respectively. For the height these values are 466.3 cm and 193.3 cm, respectively, and for the radius 217.0 cm and 90.4 cm, respectively.
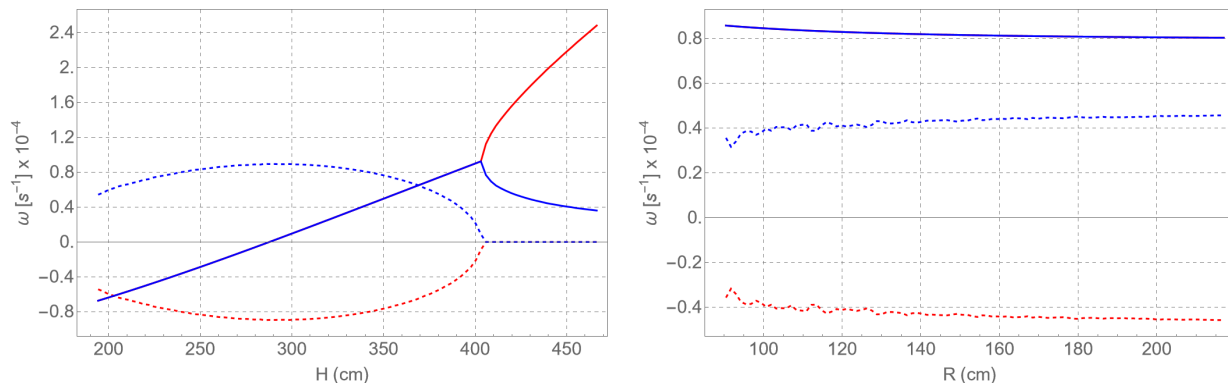
Figure 4.2: Real (solid) and imaginary(dashed) parts of the roots (blue and red resp.) of the stability coefficient ω_2 as a function of height (left) and radius (right).

As can be seen in Fig. 4.2, the larger height decreases the neutronic coupling and thus leads to the first axial harmonic mode becoming less stable (seen by an increase in the real value of the roots). At some point just above $400\,$cm the mode stops oscillating (seen by the imaginary value becoming zero) and sees only an exponential increase. Changes in the radius do not affect the stability of this mode, as long as the power is scaled with the dimension. These results support the conclusions by Obaidurrahman and Singh [13] which show that increasing height leads to less stability of the first axial harmonic.

4.3.2 Impact of Diffusion Coefficient D

The diffusion coefficient appears directly in Eq. (3.55) and in the expression for k_{eff}. In a real core, the diffusion coefficient is determined by the diffusion area L^2 as well as the absorption cross section Σ_a. As such, it is susceptible to both changes in core composition as well as temperature. Usually, a higher fuel burnup decreases the diffusion coefficient making the core more loosely coupled [20]. Higher moderator temperatures will usually slightly increase the diffusion coefficient. In this analysis, the value of Σ_a is assumed to remain constant. The maximum and minimum values for D were 130% and 70% of the nominal value corresponding to $1.28\,\mathrm{cm^2s^{-1}}$ and $0.69\,\mathrm{cm^2s^{-1}}$, respectively.

The results seen in Fig. 4.3 support the hypothesis [11, 20] that an increase in the diffusion coefficient increases the neutronic coupling within the reactor and thus has a stabilising effect (seen by a decrease in the real value of the roots) for this given mode. Increasing the diffusion coefficient has a stabilising effect for all modes.

4.3.3 Impact of Reactor Power Level

Changing the equilibrium power level while keeping the volume of the reactor constant means changing the equilibrium neutron flux which in turn affects the equilibrium xenon concentration. The power is changed between 30% and 120% of the nominal value corresponding
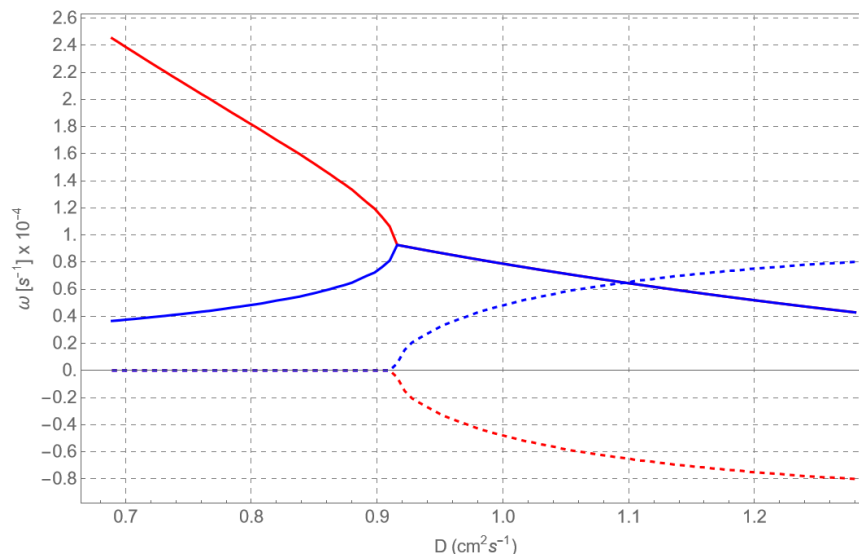
Figure 4.3: Real (solid) and imaginary(dashed) parts of the roots (blue and red resp.) of the stability coefficient ω_2 as a function of the diffusion coefficient D.

to 1.07 MW and 4.28 MW, respectively.

As seen in Fig. 4.4, increasing the reactor power decreases the stability of the mode (seen by an increase in the real value of the roots). This trend is common for all modes and supports the existing literature [21].

4.3.4 Impact of absorption cross section Σ_a

The absorption cross section Σ_a is assumed to change independently of the xenon absorption cross section and is only assumed to be caused by changes in the capture cross section. Thus, the fission cross section is assumed to be unaffected by the variation of the absorption cross section. The feedback coefficient is also assumed to be unaffected by the Σ_a changes. This parameter directly appears in Eq. (3.55) and has a contribution to k_{eff}. Σ_a is varied between 70% and 130% of its nominal value. This corresponds to numerical values of $1.6 \times 10^{-2}\,\mathrm{cm}^{-1}$ and $3.0 \times 10^{-2}\,\mathrm{cm}^{-1}$, respectively.

From Fig. 4.5 it can be seen that an increase in the absorption cross section causes an increase in the real part of the roots of the stability coefficient thereby causing the system to be less stable. Again, a point is seen where the imaginary part becomes zero and the mode no longer oscillates. The relationship between stability and Σ_a can be explained as follows. Since Σ_f and the power are kept constant, a decrease in the value of k_{eff} means that the equilibrium neutron flux must necessarily increase.

Figure 4.4: Real (solid) and imaginary(dashed) parts of the roots (blue and red resp.) of the stability coefficient ω_2 as a function of the power.
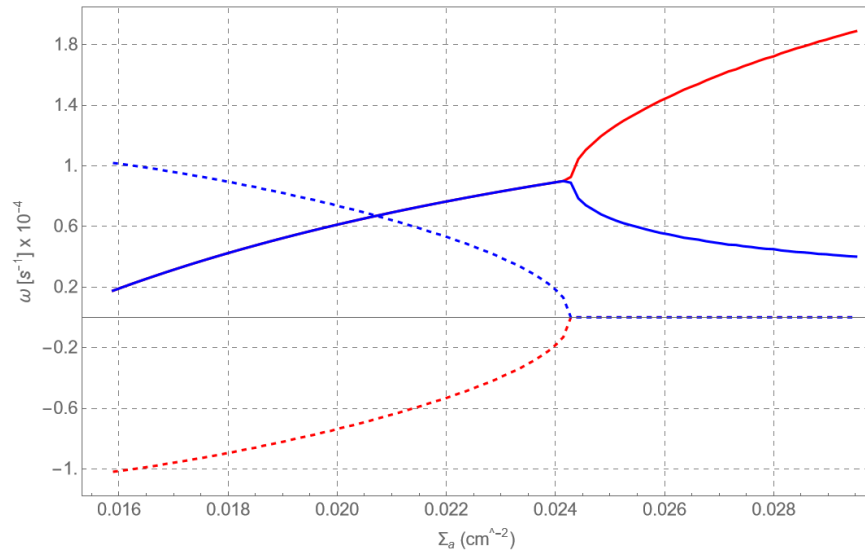
Figure 4.5: Real (solid) and imaginary (dashed) parts of the roots (blue and red resp.) of the stability coefficient ω_m as a function of the absorption cross section Σ_a.
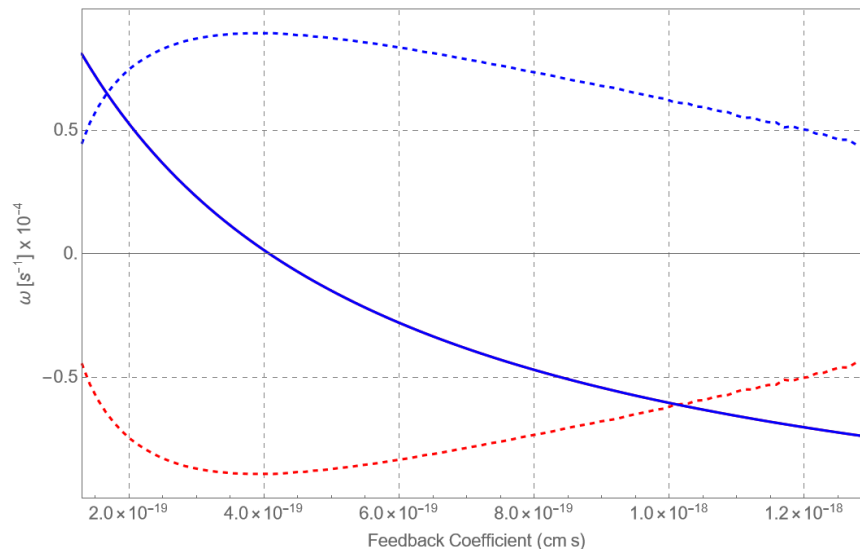
Figure 4.6: Real (solid) and imaginary (dashed) parts of the roots (blue and red resp.) of the stability coefficient ω_m as a function of the feedback coefficient $\frac{\partial \Sigma_a}{\partial \phi}$.
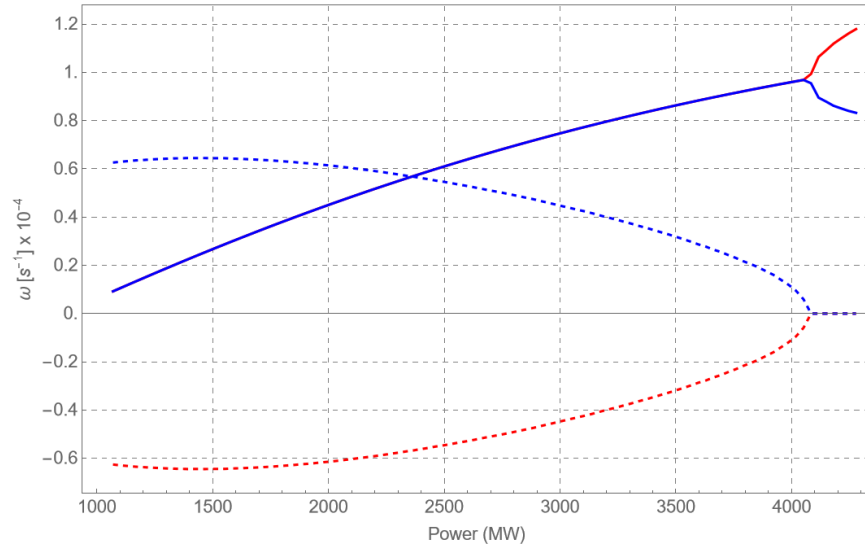
4.3.5 Impact of the feedback coefficient $\frac{\partial \Sigma_a}{\partial \phi}$

The feedback coefficient only appears in the term containing $\frac{\partial \Sigma_a}{\partial \phi} \phi_0^m$. Since a validated value is not available for the data on which the model is built, it is here a variable (i.e., tunable) parameter. Nonetheless, a realistic parameter range can be established. Several sources use the power feedback coefficient $\alpha_p = -2.69 \times 10^{-4} \, \text{cm}^{-1}$ [20, 39] which corresponds to a value of $\frac{\partial \Sigma_a}{\partial \phi} = 4.73 \times 10^{-19}$ cms. For this sensitivity analysis, the feedback coefficient is changed by one order of magnitude between the nominal value used in the sensitivity analysis and the value used in the comparison with the 2G-HET model.

The effect of varying the feedback coefficient can be seen in Fig. 4.6. An increase in the feedback coefficient causes the analysed mode to become more stable as it contributes to mitigating deviations from the equilibrium value.

4.4 Numerical Comparison between the 1G-HOM and 2G-HET models

We now turn to comparing the 1G-HOM and 2G-HET models. For the purpose of the comparison, an initial perturbation of 1% was introduced to the neutron flux in mode 2 to simulate an asymmetric reactivity insertion in the core. This corresponds to $1.5 \cdot 10^{13} \text{cm}^{-2}\text{s}^{-1}$ for the 2G-HET model and $5.9 \cdot 10^{12} \text{ cm}^{-2}\text{s}^{-1}$ for the 1G-HOM model.

In Fig. 4.7 the results of the time integration of Eqs. (2.25) to (2.27) is compared to that of
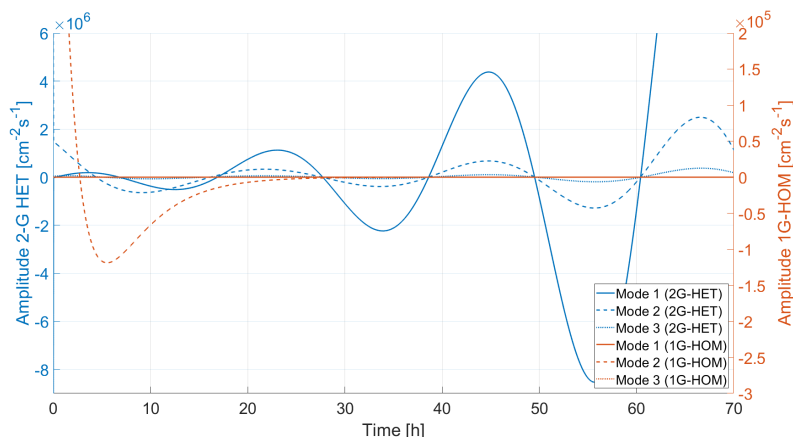
Figure 4.7: Time series of mode 1, 2 and 3 calculated with 2G-HET and 1G-HOM

Eqs. (3.16) to (3.18). Only the modes which took non-zero values are shown in the figure. The couplings in the 1G-HOM model can be seen in Fig. 2 in appendix B. In both models, no coupling between axial and radial spatial modes was seen. These results fit the existing literature which usually treats axial and radial oscillations separately [11].

The comparison between the 2G-HET and 1G-HOM models reveals substantial discrepancies in their predictions for reactor stability concerning xenon oscillations. The 2G-HET model predicts that mode 2 itself first decreases in amplitude but through their coupling perturbs mode 1 which then exhibits growing oscillations. After 40 hours, the coupling from mode 1 to modes 2 and 3 causes the amplitudes of modes 2 and 3 to increase after which all three modes exhibit divergent oscillations with mode 1 having the largest amplitude of the three modes. On the other hand, the 1G-HOM model shows the amplitude of mode 2 decaying quickly without oscillations and seemingly, without perturbing any of the other modes. Thus, the 1G-HOM model predicts a more stable system concerning xenon oscillations than the 2G-HET model. The reason behind these discrepancies is further explored in the coming sections.

4.5 Analytical Comparison

By neglecting the coupling between the modes, the parameters appearing in Eqs. (2.25) to (2.27) can be inserted into a determinant equation similar to Eq. (3.55) and the roots can be found analytically for each mode in the 2G-HET model. These are compared to the values in the 1G-HOM model in Fig. 4.8. From these results, further insight is granted into the dynamics of the individual modes without the effect of coupling. It can be seen from these figures that mode 1 from the 2G-HET model has positive real values and non-zero imaginary values indicating oscillations that grow in time. Mode 2 has slightly negative and mode 3 has larger negative real values and non-zero imaginary values indicating oscillations that decay in time. In contrast, the roots calculated in the 1G-HOM model all have negative real values and

(a) 2G-HET   **(b)** 1G-HOM
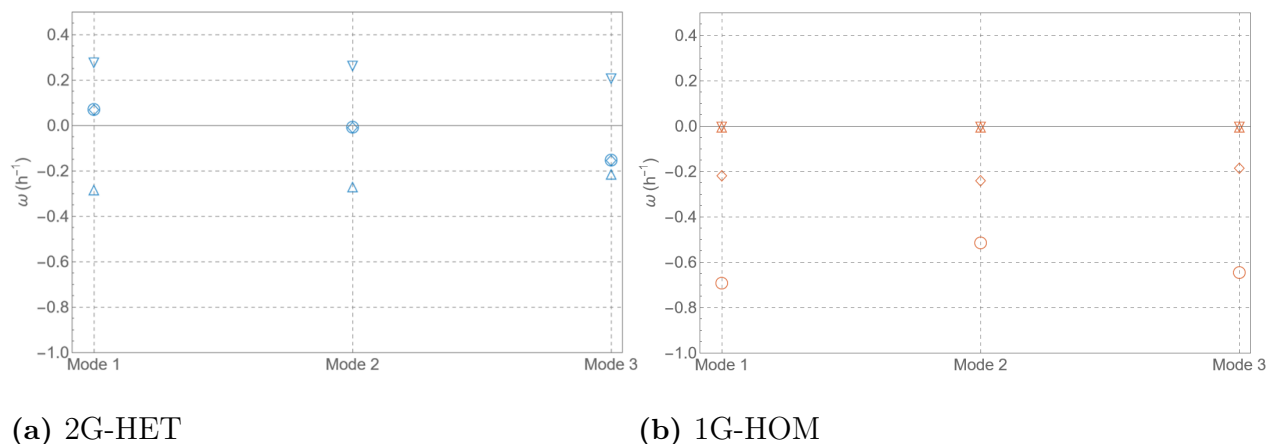
Figure 4.8: Real ($\diamond$ and $\circ$) and imaginary ($\triangle$ and $\triangledown$) parts of the roots ω_1 (blue) and ω_2 (red) of mode 2 related to the iodine-xenon oscillations.

zero-valued imaginary parts indicating all three modes will decay in time without oscillations. This indicates that for the 2G-HET model, mode 1 is driving the growing oscillations seen in Fig. 4.7 and that the other modes are growing because of a non-zero coupling to mode 1.

4.6 Eigenvalue Separation and Neutronic Coupling

The difference of the eigenvalues of the different modes with the fundamental mode, i.e., EVS $= 1/k_0 - 1/k_m$, is an indicator of the stability of a nuclear reactor according to [13]. This measure is investigated to find the possible reason behind the differences seen in stability predictions between the two models. Table 4.3 shows the effective multiplication constant (which is the same as the eigenvalue of the fundamental mode), as well as the difference between this value and the eigenvalues of the higher order modes, for both models. The values are similar between the two models for all three modes and thus a difference in the eigenvalue separation cannot be the cause for the discrepancies seen in Fig. 4.8.

Model	k_{eff}	EVS 1-2 (pcm)	EVS 1-3 (pcm)
1G-HOM	1.0397	746	2150
2G-HET	1.0375	806	2410
Difference (pcm)	-22	60	260

Table 4.3: Effective multiplication factor and EVS for the first and second axial harmonics.

4.7   Mode Coupling Comparison

In this section, the terms that couple one mode to all other modes are compared between the two models. The coupling between the m-th mode with the n-th modes (with m, n = 0, 1, ..., N) appears in the second and third RHS terms of Eq. (2.25), and in the third and last RHS terms of Eq. (2.27). These four terms have sums of inner products between modes. Three of them contain the equilibrium neutron flux $\Phi_{eq}(\mathbf{r})$ and one contains the equilibrium xenon concentration X_{eq}. Since the terms with $\Phi_{eq}(\mathbf{r})$ have similar couplings, the comparison is only taken for the following terms:

$$\frac{\left\langle\hat{\Phi}_m^\dagger(\mathbf{r})\middle|\boldsymbol{\Phi}_{eq}(\mathbf{r})\times\hat{\Phi}_n(\mathbf{r})\right\rangle}{\left\langle\hat{\Phi}_m^\dagger(\mathbf{r})\middle|\mathbf{v}^{-1}\times\hat{\Phi}_m(\mathbf{r})\right\rangle}=\frac{\int_V\left(\phi_{1,m}^\dagger(\mathbf{r})\Phi_{1,eq}(\mathbf{r})\phi_{1,n}(\mathbf{r})+\phi_{2,m}^\dagger(\mathbf{r})\Phi_{2,eq}(\mathbf{r})\phi_{2,n}(\mathbf{r})\right)dV}{\int_V\left(\phi_{1,m}^\dagger(\mathbf{r})v_1^{-1}\phi_{1,m}(\mathbf{r})+\phi_{2,m}^\dagger(\mathbf{r})v_2^{-1}\phi_{2,m}(\mathbf{r})\right)dV}$$

(4.3)

$$\frac{\left\langle\hat{\Phi}_m^\dagger(\mathbf{r})\middle|\bar{\mathbf{X}}\times X_{eq}(\mathbf{r})\times\hat{\Phi}_n(\mathbf{r})\right\rangle}{\left\langle\hat{\Phi}_m^\dagger(\mathbf{r})\middle|\hat{\Phi}_m(\mathbf{r})\right\rangle}=\frac{\int_V\phi_{1,m}^\dagger(\mathbf{r})X_{eq}(\mathbf{r})\phi_{2,n}(\mathbf{r})dV}{\int_V\left(\phi_{1,m}^\dagger(\mathbf{r})\phi_{1,m}(\mathbf{r})+\phi_{2,m}^\dagger(\mathbf{r})\phi_{2,m}(\mathbf{r})\right)dV}$$

(4.4)

The value of the terms is normalised to the self-coupling of mode 1 for easier comparison.

Mode	m = 1	m = 2	m = 3
n = 1	1	0.11	0.12
n = 2	0.09	0.83	0.10
n = 3	0.10	0.10	0.83

(a) 2G-HET Eq. (4.3) term

Mode	m = 1	m = 2	m = 3
n = 1	1	0.03	0.02
n = 2	0.02	0.95	0.03
n = 3	0.02	0.03	0.95

(b) 2G-HET Eq. (4.4) term

Mode	m = 1	m = 2	m = 3
n = 1	1	0.00	0.20
n = 2	0.00	0.80	0.00
n = 3	0.20	0.00	0.77

(c) 1G-HOM equivalent Eq. (4.3) term

Mode	m = 1	m = 2	m = 3
n = 1	1	0.00	0.02
n = 2	0.00	0.98	0.00
n = 3	0.02	0.00	0.96

(d) 1G-HOM equivalent Eq. (4.4) term

Table 4.4: Amplitude of the normalized coupling coefficients for modes 1, 2 and 3.

In Table 4.4, several notable observations are made regarding the couplings between different modes in both the neutron (Eq. (4.3)) and xenon (Eq. (4.4)) terms of the 2G-HET and 1G-HOM models.

Firstly, in the 2G-HET model, there exists a coupling between mode 2 and modes 1 and 3 for both the neutron and xenon terms. However, this coupling is negligible in the 1G-HOM

model. This difference in couplings between the two models suggests that the 2G-HET model incorporates interactions between these modes that are not accounted for in the 1G-HOM model.

Secondly, the coupling between modes 1 and 3 is larger in the 1G-HOM model compared to the 2G-HET model. Both of these discrepancies are attributed to the difference in spatial refinement between the models and the equilibrium axial offset. Further investigation of these factors is done in Section 4.9, providing deeper insights into the differences between the two models and their treatment of mode couplings.

4.8   Effect of Energy Refinement

The differences between the 2G-HET and 1G-HOM models are found to be larger for the terms containing inner products between modes. The terms containing the equilibrium neutron flux in 1G-HOM are up to 3 times larger than the corresponding terms in 2G-HET. This section explores the effect of going from one energy group to two energy groups by creating a two-group homogeneous model and comparing the relationship between Eq. (4.3) and Eq. (4.4) to the 2G-HET and 1G-HOM model. Only the inner products with $m = n$ are considered for modes 1, 2 and 3 hereafter.

A one-dimensional homogeneous two-group formulation is employed with the following expressions for the adjoint and forward neutron flux vectors.

$$\left\langle \phi_m^\dagger \right|^T = A^\dagger \begin{bmatrix} 1 \\ \frac{\nu\Sigma_{f,2}/k_{eff}^\dagger}{D_2 B_{g,m}^2 + \Sigma_{a,2}} \end{bmatrix} \begin{cases} \cos(B_{g,m}z) & n = 0,2,4... \\ \cos(B_{g,m}z + \pi/2) & n = 1,3,5... \end{cases} \tag{4.5}$$

$$|\phi_n\rangle = A \begin{bmatrix} 1 \\ \frac{\Sigma_r}{D_2 B_{g,n}^2 + \Sigma_{a,2}} \end{bmatrix} \begin{cases} \cos(B_{g,n}z) & n = 0,2,4... \\ \cos(B_{g,n}z + \pi/2) & n = 1,3,5... \end{cases} \tag{4.6}$$

where $2a$ is the length of the system and $B_{g,n} = \frac{(n+1)\pi}{2a}$. The origin of the system is taken at the centre of the core. The equilibrium flux and xenon concentration used in the homogenization are derived from the forward flux scaled with the reactor power.

Table 4.5 provides a summary of the ratios between the terms corresponding to Eqs. (4.3) and (4.4) with $n = m$ for the three different models. Comparing the two-group heterogeneous (2G-HET) and two-group homogeneous (2G-HOM) values, it is evident that spatial homogenization does not significantly affect the inner products for any of the three modes. However, the energy condensation has a notable impact on the difference between the 2G-HOM and 1G-HOM values.

This highlights the significance of energy condensation in capturing the behaviour of xenon oscillations. As Xe-135 only absorbs neutrons in the thermal range, refining the model energy discretisation has a large impact on the stability predictions.

Model	Mode 1	Mode 2	Mode 3
2G-HET $(\cdot 10^6)$	1.13	0.99	0.99
2G-HOM $(\cdot 10^6)$	1.20	0.99	0.99
1G-HOM $(\cdot 10^6)$	3.26	2.66	2.57

Table 4.5: Ratio between terms corresponding to Eqs. (4.3) and (4.4) with $n = m$ showing the effect of spatial homogenization vs. condensation of energy groups

4.9 Effect of Spatial Refinement

This section investigates the effect of spatial refinement and axial offset (AO) on the stability of the system when transitioning from a homogeneous model to a heterogeneous model.

The heterogeneous data was prepared with a large equilibrium axial offset ($EAO = -20.5\%$) (with the axial offset defined in Eq. (1.3)) and a very small equilibrium radial offset ($ERO = 7 \cdot 10^{-4}\%$). This means that the power is 20.5% higher at the bottom of the core compared to the top but that the power is close to equal between one half of the radial plane of the core compared to the other.

To investigate the effect of the axial offset on the coupling terms, the normalized axial profiles from Eqs. (4.3) and (4.4) and the corresponding terms for the 1G-HOM model for $m = 1$ and $n = 1, 2$, and 3, respectively, are visualized. These profiles are averaged over plane B (see Figure 4.1) and compared with the profiles obtained from the equivalent terms in the 1G-HOM model. The values of the corresponding coupling coefficients from Table 4.4 are also reported in Figures 4.9 to 4.11, with legends referring to Tables 4.4a to 4.4d, respectively.

The results show that the axial profiles estimated with the 2G-HET model closely reflect the axial power offset, with more pronounced peaking in the bottom part of the core. In contrast, the 1G-HOM profiles are symmetrical or anti-symmetrical to the mid-elevation line. Resolving the spatial heterogeneity and incorporating the power offsets lead to the breaking of symmetry or anti-symmetry in the integrands of the inner products for the coupling coefficients. As a consequence, the calculated values of the coupling coefficients between modes with $m \neq n$ differ from those calculated in the 1G-HOM model.
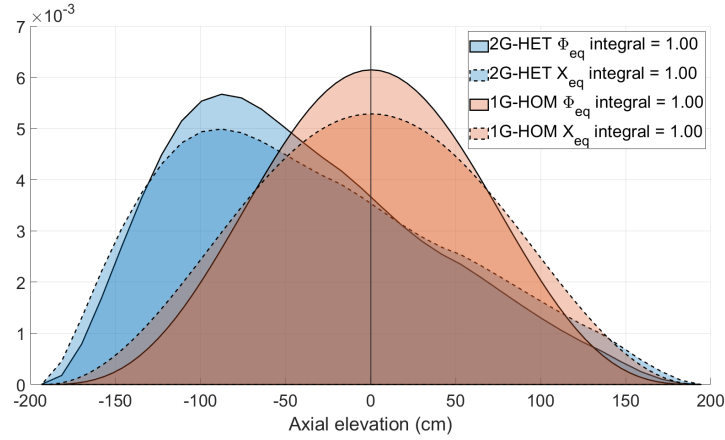
Figure 4.9: Axial profile extracted from the inner product of the coupling coefficients for m = 1 and n = 1.
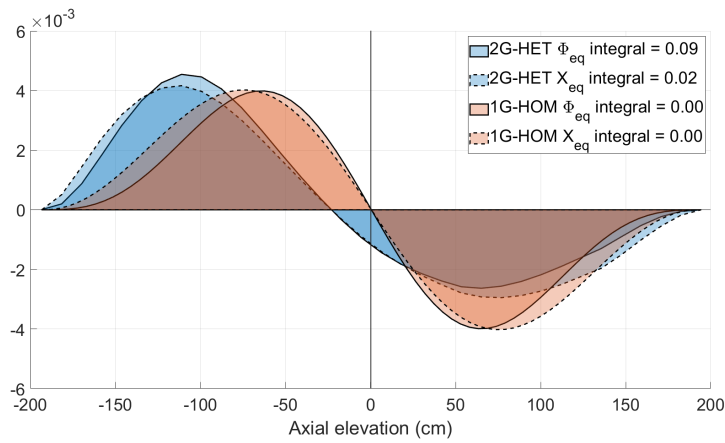
Figure 4.10: Axial profile extracted from the inner product of the coupling coefficients for m = 1 and n = 2.
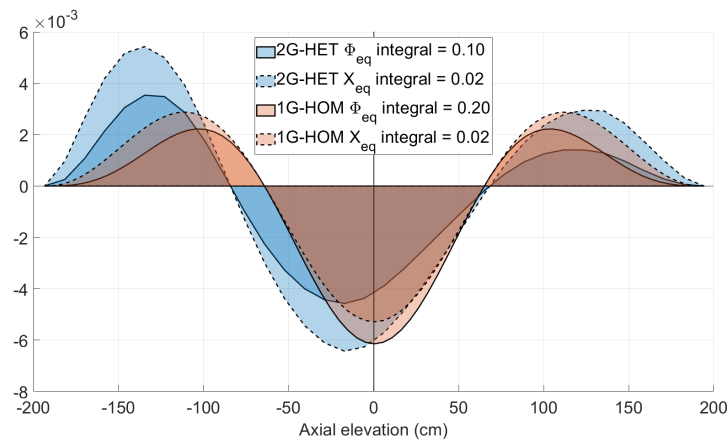
Figure 4.11: Axial profile extracted from the inner product of the coupling coefficients for m = 1 and n = 3.

5

Conclusion and Outlook

5.1 Conclusion

In this thesis, two different three-dimensional intrusive reduced order models (ROM) were presented for predicting the stability of a reactor core concerning xenon oscillations under various conditions: the two-group heterogeneous (2G-HET) and the one-group homogeneous (1G-HOM). Both ROMs were created starting from the underlying equations of the neutron flux, written in a diffusion approximation, and the equations expressing the balance in the iodine and xenon concentrations, respectively. The quantities of interest were rewritten into changes from their equilibrium values and were then expanded into a sum of N spatial eigenmodes of the forward diffusion problem multiplied with a time-dependent amplitude. This method changed the set of partial differential equations, which were challenging to solve, into a larger set of coupled ordinary differential equations, which were easier to solve. This new set of balance equations provided details of the physical behaviour by dissecting the time signal into its constituent modes. The method allowed for sensitivity analysis of the effect of changing parameters on each mode individually, providing a tool for enhancing the physical understanding of the system.

Actual nuclear reactor core configurations are significantly heterogeneous. This heterogeneity varies both over short time periods with control rod insertions and boron injections and over long periods with core burnup. In this thesis, capturing the heterogeneity of the core was investigated in the terms that differed the most between the two models. It was shown that the heterogeneity of the core had a significant effect on the coupling between the dynamic modes of the system especially when spatial offsets were present. This effect had a crucial effect on the development of xenon oscillations within the core. particularly for anti-symmetric axial distribution, the effect of refining the axial offset caused the integrals over the volume to become non-zero in contrast to the 1G-HOM model.

The thesis also investigated the effect of energy condensation by developing an additional two-group homogeneous model (2G-HOM) and calculating the ratios between the self-coupling terms of the three models (1G-HOM, 2G-HOM, and 2G-HET). In this way, any constant which may differ between the models should cancel out. The analysis showed that energy condensation had a much more significant effect on the self-coupling terms than the spatial

refinement. As a result, energy refinement was the most significant source of difference in the prediction of stability of isolated modes between the models.

The sensitivity analysis conducted in the thesis, shed light on the relevance of each model parameter and its influence on the stability concerning xenon oscillations.

In conclusion, this research contributed to a better understanding of nuclear reactor stability and provided valuable tools for the evaluation of reactor operation and safety measures during flexible load following conditions.

5.2 Outlook

The research work planned for the continuation of the project, will address the items below.

5.2.1 Splitting the Model

In the literature and this work, it is noted that the axial and radial modes developed mostly independently. For this reason, it might be advantageous to separate the three-dimensional ROM into one model predicting axial oscillations and one predicting radial oscillations. This would limit the number of modes needed to be included for each model and reduce the complexity of the models while retaining the physical behaviour, thus increasing efficiency.

5.2.2 Developing a Data-Driven POD ROM

Data-driven, non-intrusive ROM methods based on the proper orthogonal decomposition (POD) will be studied. These models are solely based on data from either experiments or high-fidelity simulations with the advantage of not needing access to the underlying equations. For this reason, more information about thermal-hydraulics will be included in the model as opposed to the simple thermal feedback term that was included in the present models. In principle, some thermal-hydraulic equations could be implemented in the intrusive model but access to the thermal-hydraulic relations for a specific core is seldom available as this information is proprietary.

5.2.3 Sampling a Larger Parameter Space

The intrusive models should be sampled from a broader parameter space, spanning all relevant configurations with denser sampling points in areas where xenon oscillations are likely to occur. Using interpolation methods, efficient predictions are possible for all core configurations within the sampled space. This also unlocks the opportunity to make sensitivity analysis and uncertainty quantification possible. This is where the true strength of reduced order modelling lies.

5.2.4 Validation

The models presented in this thesis have not yet been assessed against high-fidelity legacy codes. Such comparison is strictly necessary before any final conclusions can be drawn from the models about reactor stability concerning xenon oscillations. At present, data from Simulate 5 (which is a reactor core simulator widely used for commercial light water reactors) is being prepared and collected with the help of Ringhals nuclear power plant to validate the predictions made by the models.

Bibliography

[1] International Energy Agency. *Nuclear Power and Secure Energy Transitions: From today's challenges to tomorrow's clean energy systems*. en. OECD, Aug. 2022. DOI: 10.1787/aca1d7ee-en. URL: https://www.oecd-ilibrary.org/energy/nuclear-power-and-secure-energy-transitions_aca1d7ee-en (visited on 04/27/2023).

[2] *World Energy Outlook 2022*. en. Paris: IEA, 2022. URL: https://www.iea.org/reports/world-energy-outlook-2022.

[3] *IEA*. May 17, 2023. URL: https://www.iea.org/countries/sweden.

[4] Jonas Persson et al. *Lastföljning i Kärnkraftverk*. Report. Elforsk, Dec. 2011.

[5] Maja Lundback. *Kärnkraftens Roll i Kraftsystemet*. Report. Svenska Kraftnät, Oct. 2018.

[6] Christophe Demazière. *Physics of Nuclear Reactors (Textbook)*. Chalmers University of Technology, Gothenburg, 2017.

[7] D.A. Brown et al. "ENDF/B-VIII.0: The 8 th Major Release of the Nuclear Reaction Data Library with CIELO-project Cross Sections, New Standards and Thermal Scattering Data". en. In: *Nuclear Data Sheets* 148 (Feb. 2018), pp. 1–142. ISSN: 00903752. DOI: 10.1016/j.nds.2018.02.001. URL: https://linkinghub.elsevier.com/retrieve/pii/S0090375218300206 (visited on 06/16/2023).

[8] U.S. Department of Energy. *DOE Fundamentals Handbook. Nuclear Physics and Reactor Theory*. Vol. 2. U.S. Department of Energy, Jan. 1993.

[9] Bertrand Mercier et al. "Modeling and control of xenon oscillations in thermal neutron reactors". en. In: *EPJ Nuclear Sciences & Technologies* 6 (2020), p. 48. ISSN: 2491-9292. DOI: 10.1051/epjn/2020009. URL: https://www.epj-n.org/10.1051/epjn/2020009 (visited on 10/26/2022).

[10] Jae Seung Song and Nam Zin Cho. "Two-Group, Flux-Coupled Xenon Oscillation Model with an Equation System of Axial Difference Parameters". en. In: *Nuclear Technology* 119.2 (Aug. 1997), pp. 105–111. ISSN: 0029-5450, 1943-7471. DOI: 10.13182/NT97-A35379. URL: https://www.tandfonline.com/doi/full/10.13182/NT97-A35379 (visited on 10/26/2022).

[11] John C. Lee. *Nuclear Reactor: Physics and Engineering*. 1st ed. Wiley, Feb. 2020.

[12] M Hone et al. "AP1000 Core Reference Report". en. In: (2012).

[13] K. Obaidurrahman and Om Pal Singh. "Spatial neutronic coupling aspects in nuclear reactors". en. In: *Nuclear Engineering and Design* 240.10 (Oct. 2010), pp. 2755–

2760. ISSN: 00295493. DOI: 10.1016/j.nucengdes.2010.05.004. URL: https://linkinghub.elsevier.com/retrieve/pii/S0029549310003213 (visited on 12/12/2022).

[14]   Michele S. Gerber and Brian Casserly. *National Historic Landmark Nomination - B Reactor*. National Historic Landmarks Survey, Feb. 2007.

[15]   DOE. *B-Reactor*. URL: https://www.hanford.gov/page.cfm/BReactor. (accessed: 23/08/2023).

[16]   Jeff Brown. "Secret Weapon: The Hanford B Reactor". In: *Civil Engineering Magazine* 85.10 (2015), pp. 40–43. DOI: 10.1061/ciegag.0001043. eprint: https://ascelibrary.org/doi/pdf/10.1061/ciegag.0001043. URL: https://ascelibrary.org/doi/abs/10.1061/ciegag.0001043.

[17]   Mikhail V. MALKO. "The Chernobyl Reactor: Design Features and Reasons for Accident". en. In: *Recent Research Activities about the Chernobyl NPP Accident in Belarus, Ukraine and Russia* (2002), pp. 11–27.

[18]   Bertrand Mercier et al. "A simplified analysis of the Chernobyl accident". en. In: *EPJ Nuclear Sciences & Technologies* 7 (2021), p. 1. ISSN: 2491-9292. DOI: 10.1051/epjn/2020021. URL: https://www.epj-n.org/10.1051/epjn/2020021 (visited on 06/10/2023).

[19]   Evans D. Kitcher and Sunil S. Chirayath. "A neutron transport and thermal hydraulics coupling scheme to study xenon induced power oscillations in a nuclear reactor". en. In: *Annals of Nuclear Energy* 106 (Aug. 2017), pp. 64–70. ISSN: 03064549. DOI: 10.1016/j.anucene.2017.03.045. URL: https://linkinghub.elsevier.com/retrieve/pii/S0306454916308933 (visited on 06/11/2023).

[20]   K. Obaidurrahman and J.B. Doshi. "Spatial instability analysis in pressurized water reactors". en. In: *Annals of Nuclear Energy* 38.2-3 (Feb. 2011), pp. 286–294. ISSN: 03064549. DOI: 10.1016/j.anucene.2010.10.015. URL: https://linkinghub.elsevier.com/retrieve/pii/S0306454910003841 (visited on 12/12/2022).

[21]   Rashdan Talal Al Malkawi, Sergey B. Vygovsky, and Osama Wasef Batayneh. "Investigation of the impact of steady-state VVER-1000 (1200) core characteristics on the reactor stability with respect to xenon oscillations". In: *Nuclear Energy and Technology* 6 (2020), pp. 289–294.

[22]   G.S. Chang. "Advanced CANDU reactors axial xenon oscillation controllability validation". en. In: *Annals of Nuclear Energy* 96 (Oct. 2016), pp. 441–445. ISSN: 03064549. DOI: 10.1016/j.anucene.2016.06.039. URL: https://linkinghub.elsevier.com/retrieve/pii/S0306454916304820 (visited on 06/10/2023).

[23]   P.K. Doshi and R. W. Miller. *An Investigation of Axial Xenon Stability in VVER-1000 Reactor Designs*. 1993.

[24]   U.S.Nuclear Regulatory Commission. *R325C CE Technology Cross Training*. U.S.Nuclear Regulatory Commission. Chap. 14. URL: https://www.nrc.gov/docs/ML1125/ML11251A047.pdf.

[25]   Yoichiro Shimazu. "Continuous Guidance Procedure for Xenon Oscillation Control". In: *Journal of Nuclear Science and Technology* 32.2 (Feb. 1995), pp. 95–100.

[26]   Gholam Reza Ansarifar and Saeed Saadatzi. "Nonlinear control for core power of pressurized water nuclear reactors using constant axial offset strategy". en. In: *Nu-*

clear Engineering and Technology 47.7 (Dec. 2015), pp. 838–848. ISSN: 17385733. DOI: 10.1016/j.net.2015.09.002. URL: https://linkinghub.elsevier.com/retrieve/pii/S1738573315001710 (visited on 10/26/2022).

[27] Gašper Žerovnik et al. "An overview of power reactor kinetics and control in load-following operation modes". en. In: *Frontiers in Energy Research* 11 (Feb. 2023), p. 1111357. ISSN: 2296-598X. DOI: 10.3389/fenrg.2023.1111357. URL: https://www.frontiersin.org/articles/10.3389/fenrg.2023.1111357/full (visited on 06/12/2023).

[28] A. M. Christie and C. G. Poncelet. "On the Control of Spatial Xenon Oscillations". en. In: *Nuclear Science and Engineering* 51.1 (May 1973), pp. 10–24. ISSN: 0029-5639, 1943-748X. DOI: 10.13182/NSE73-A23253. URL: https://www.tandfonline.com/doi/full/10.13182/NSE73-A23253 (visited on 10/26/2022).

[29] E.E.Utley. *Letter from Carolina Power and Light Company to the U.S. Atomic Energy Commission on Divergent Axial Xenon Oscillations.* Oct. 1972.

[30] Steven L. Brunton and J. Nathan Kutz. *Data-Driven Science and Engineering: Machine Learning, Dynamical Systems, and Control.* en. 1st ed. Cambridge University Press, Jan. 2019. ISBN: 978-1-108-42209-3. DOI: 10.1017/9781108380690. URL: https://www.cambridge.org/core/product/identifier/9781108380690/type/book (visited on 06/13/2023).

[31] Wilhelmus H.A. Schilders, Henk A. van der Vorst, and Joost Rommes. *Model Order Reduction. Theory, Research Aspects and Applications.* Springer, 2008. ISBN: 978-3-540-78840-9. DOI: 10.1007/978-3-540-78841-6.

[32] Fahad Alsayyari et al. "A fully adaptive nonintrusive reduced-order modelling approach for parametrized time-dependent problems". en. In: *Computer Methods in Applied Mechanics and Engineering* 373 (Jan. 2021), p. 113483. ISSN: 00457825. DOI: 10.1016/j.cma.2020.113483. URL: https://linkinghub.elsevier.com/retrieve/pii/S004578252030668X (visited on 10/26/2022).

[33] Fahad Alsayyari et al. "A nonintrusive adaptive reduced order modeling approach for a molten salt reactor system". en. In: *Annals of Nuclear Energy* 141 (June 2020), p. 107321. ISSN: 03064549. DOI: 10.1016/j.anucene.2020.107321. URL: https://linkinghub.elsevier.com/retrieve/pii/S0306454920300190 (visited on 08/22/2023).

[34] Robert Nowlan. *Joseph Fourier.* URL: https://web.archive.org/web/20160304034040/http://www.robertnowlan.com/pdfs/Fourier,%20Joseph.pdf. (accessed: 23/08/2023).

[35] Todd Ehret. "Old Brass Brains. Mechanical prediction of tides". In: *ACSM Bulletin* (June 2008).

[36] British Association for the Advancement of Science. *William Thomson's Tide Predicting Machine, 1872.* URL: https://collection.sciencemuseumgroup.org.uk/objects/co53901/william-thomsons-tide-predicting-machine-1872-tide-predictor. (accessed: 23/08/2023).

[37] John P. Boyd. *Chebyshev and Fourier Spectral Methods.* 2nd ed. DOVER Publications, Inc., 2000.

[38] S. Nakamura. *Computational methods in engineering and science with applications to fluid dynamics and nuclear systems.* en. John Wiley and Sons, Jan. 1977.

[39]   Jae Seung Song, Nam Zin Cho, and Sun Quun Zee. "Analytic Modelling of the Xenon Oscillation Due to Control Rod Movement". In: *Journal of the Korean Nuclear Society* 31.1 (Feb. 1999), pp. 80–87.

[40]   Tomasz Kozlowski and Thomas J. Downar. "OECD/NEA and U.S. NRC PWR MOX/UO2 core transient benchmark". In: *OECD Nuclear Energy Agency report, Final Specifications, Revision 2* (2003).